

CHELSA-TraCE21k v1.0. Downscaled transient temperature and precipitation data since the last glacial maximum

Dirk Nikolaus Karger¹, Michael P. Nobis¹, Signe Normand², Catherine H. Graham¹, Niklaus E. Zimmermann¹

¹Swiss Federal Research Institute WSL, Zürcherstrasse 111, 8903 Birmensdorf, Switzerland

²Aarhus University, Ny Munkegade 116, 8000 Aarhus, Denmark

Correspondence to: Dirk N. Karger (dirk.karger@wsl.ch)

Abstract. High resolution, downscaled climate model data are used in a wide variety of applications across environmental sciences. Here we introduce the CHELSA-TraCE21k downscaling algorithm to create global monthly climatologies for temperature and precipitation at 30-arc sec spatial resolution in 100-year time steps for the last 21,000 years. Paleo orography at high spatial resolution and at each timestep is created by combining high resolution information on glacial cover from current and Last Glacial Maximum (LGM) glacier databases with the interpolation of and interpolations using a dynamic ice sheet model (ICE6G) and a coupling to mean annual temperatures from TraCE-21k (Transient Climate Evolution of the last 21,000 years) based on the Community Climate System Model version 3 (CCSM3-TraCE21k). Based on the reconstructed paleo orography, mean annual temperature and precipitation was downscaled using the CHELSA (Climatologies at high resolution for the Earth's land surface areas) V1.2 algorithm. The data were validated by comparisons with the glacial extent of the Laurentide ice shield sheet based on expert delineations, proxy data from Greenland ice cores, historical climate data from meteorological stations, and a dynamic simulation of species distributions throughout the Holocene. Validations show that CHELSA-TraCE21k output creates a reasonable representation of the distribution of temperature and precipitation through time at a high spatial resolution, and simulations based on the data are capable of detecting effective known LGM refugia of species.

1 Introduction

Since the Last Glacial Maximum (LGM), variation in climate has caused multiple changes of the Earth surface, including the rearrangement of species distributions, or even extinctions (Adams and Faure, 1997; Binney et al., 2017; Prentice et al., 1991; Velichko et al., 1997; Williams et al., 2004; Yu et al., 2010). species extinctions (Prentice et al., 1991; Velichko et al., 1997; Adams and Faure, 1997; Williams et al., 2004; Yu et al., 2010; Binney et al., 2017). Yet we have not fully evaluated the historical underpinnings of these changes as we have often lacked the climate data at the necessary spatial resolution. Biological entities such as species usually encounter climatic conditions at spatial resolutions ($< 1 \text{ km}^2$) $< 1 \text{ km}$ (Seo et al., 2009) that are not captured by is beyond the spatial resolution of numerical global circulation models (GCMs) which run at much coarser grains (e.g. $> 0.5^\circ$). For many applications such as inference of ecological niches (Hutchinson, 1957), determination

of growing seasons (McMaster and Wilhelm, 1997), identification of species migrations (Engler and Guisan, 2009), or modelling of high resolution species distributions (Guisan and Thuiller, 2005; Guisan and Zimmermann, 2000), temporal and spatial variability in temperature and precipitation is highly important. For such analyses, errors (Guisan and Zimmermann, 2000; Guisan and Thuiller, 2005), temporal and spatial variability in temperature and precipitation is of utmost importance. For such analyses, imprecisions in the underlying climate data can strongly deteriorate the analytical power (Soria-Auza et al., 2010).

For the recent past the gap between the coarse GCM resolution and the high resolution needed has been bridged using satellite data (Biasutti et al., 2011; Funk et al., 2015; Huffman et al., 2007). For the recent past, the gap between the coarse GCM resolution and the high resolution needed for many ecological applications has been bridged using statistical downscaling (Karger et al., 2017a, 2020; Maraun et al., 2010; Schmidli et al., 2006; Wilby et al., 1998; Wood et al., 2004) (Wilby et al., 1998; Wood et al., 2004; Schmidli et al., 2006; Maraun et al., 2010; Karger et al., 2017a, 2020), dynamical downscaling (Skamarock et al., 2019), or interpolation of meteorological station data (Daly et al., 1997; Harris et al., 2020; Hijmans et al., 2005; Meyer-Christoffer et al., 2015). While all of these methods work comparably well for current climatic conditions, satellite or (Daly et al., 1997; Hijmans et al., 2005; Meyer-Christoffer et al., 2015; Harris et al., 2020). While all of these methods work comparably well for current climatic conditions, station data are not available before the 19th Century (end of the 20th century for satellite data), hampering an application of said methods to paleo-climatic models. Most paleoclimatic data at high spatial resolution is therefore based on climatologically aided interpolation (or change factor method) of GCM output (Brown et al., 2018). This process uses the high-resolution information of current day climatologies, and adds an interpolated anomaly derived from a coarser-resolution GCM (Hunter and Meentemeyer, 2005; Willmott and Robeson, 1995) (Willmott and Robeson, 1995; Hunter and Meentemeyer, 2005). While this approach works rather well for short term time series where topography is relatively stable (Daly et al., 1997), it becomes difficult/impractical for longer time series where the dependence structure between variables (e.g. topography and climate) is dynamic (Maraun, 2013). This phenomenon is of concern especially in the last 21'000 years, as the topography in many regions on earth has changed drastically due to the retreating ice shields/sheets and glaciers along the poles in polar regions and in high mountain areas (Scotese, 2001). While numerical climate models are able to simulate paleo-environmental conditions comparably well (Sepulchre et al., 2020), they are however, computationally very demanding, and therefore they have not been applied on ecologically relevant spatial resolutions of ~1km yet. Current global kilometer-scale models only show a simulation throughput of 0.043 SYPD (simulated years per day) (Führer et al., 2018), which is 25-fold lower than computer/computational efficient simulations of 1 SYPD (Schär et al., 2019; Schulthess et al., 2018) (Schulthess et al., 2018; Schär et al., 2019). Even with state-of-the-art supercomputers and climate models this gap can only be minimized by a factor of 20 (Neumann et al., 2019).

Climate impact studies however, often only use a reduced set of climate variables compared to those available from the output of numerical/output of climate models (Frieler et al., 2017). Such studies do not need therefore not need a complete representation of all climate processes at high spatial resolution. In ecological studies, for instance, precipitation is often used along with minimum and maximum temperatures for analyses of species occurrences (Woodward et al., 1990). Also, it is

65 common practice to describe species ranges by their climate envelopes ~~and building, thus~~ species distribution models (SDMs)
~~with are often built using~~ a relatively small set of climate predictors based on monthly minimum and maximum temperature
and precipitation (Guisan and Zimmermann, 2000; Guisan and Thuiller, 2005; ~~Guisan and Zimmermann, 2000~~).
Here we present paleo-climatic data, downscaled from the CCSM3_TraCE21k model to a 30 ~~aresec-arc sec~~. resolution using
the CHELSA V1.2 algorithm (Karger et al., 2017a), which covers time steps of 100 years from 21k-BP to 1990; ~~(TraCE-21k)~~.
70 for minimum and maximum temperatures, surface precipitation, and paleo-orography.

2 Input data

2.1 Transient climate simulations: ~~CCSM3~~ TraCE-21k

~~The CCSM3 TraCE-21k~~The TraCE-21k (Transient climate evolution of the last 21,000 years) simulation using the CCSM3
(Community Climate System Model Version 3) climate model (Carlson et al., 2012; He, 2011; Liu et al., 2009; Marcott et al.,
2011)(Liu et al., 2009; He, 2011; Marcott et al., 2011; Carlson et al., 2012) provides information on climate change over the
75 last 21,000 years, i.e. from Last Glacial Maximum (LGM) to present. The TraCE-21k ~~simulations are capable to~~
~~reproducesimulation reproduces~~ many main features of post-glacial climate dynamics in various parts of the world from low
to high latitudes and ~~includingincludes~~ abrupt climate changes (He, 2011; Liu et al., 2009). ~~CCSM3 TraCE-21k uses the~~
~~Community Climate System Model version 3 (CCSM3) of the National Center for Atmospheric Research (NCAR), which is a~~
80 ~~global climate model with coupled ocean, atmosphere, sea ice, and land surface components (Collins et al., 2006). CCSM3~~
~~TraCE-21k was calculated at~~(Liu et al., 2009; He, 2011). The TraCE-21k simulation was calculated at a T31_gx3v5 resolution
(Otto-Bliesner et al., 2006) using a coarse resolution dynamic global vegetation model (DGVM) together with the Community
Atmospheric Model 3 (CAM3), on 26 vertical hybrid coordinate levels. The land and atmosphere model ~~useuses~~ the same
resolution. The parameterizations of ~~dynamic vegetation model is the~~ DGVM ~~are~~ largely based on the Lund-Potsdam-Jena
85 (LPJ)-DGVM. The ocean model in CCSM3 ~~TraCE21k~~ uses the NCAR (National Center for Atmospheric Research) version
of the Parallel Ocean Program (POP) with 25 vertical levels and the sea ice model is the NCAR Community Sea Ice Model
(CSIM).

2.2 Observational climatology: CHELSA V1.2

CHELSA ~~is a high-resolution (30 aresec) climate data set for earth land surface areas (Karger et al., 2017b, 2017a). It includes~~
90 ~~monthly mean temperature and precipitation grids for the time period 1979-2013. CHELSA uses a quasi-mechanistical~~
~~statistical downscaling of the ERA~~(Climatologies at high resolution for the Earth's land surface areas) V1.2 is a high-resolution
(30-arc sec.) climate data set for earth land surface areas (Karger et al., 2017b). It includes mean monthly daily 2m mean,
minimum, and maximum temperature, and monthly precipitation fields at 30 -arc sec resolution for the time period 1979-2013.
CHELSA V1.2. is calculated on the CHELSA mechanistic climate downscaling model (Karger et al., 2017a), using the ERA

Field Code Changed

Formatted: English (United Kingdom)

Formatted: English (United Kingdom)

Formatted: English (United Kingdom)

95 [\(European Reanalysis\)](#) interim reanalysis (Berrisford et al., 2009) ~~with a GPCC as~~ forcing data and GPCC (Global Precipitation Climatology Center) data (Meyer-Christoffer et al., 2015) [for its](#) bias correction.

2.2 Transient glacial extent simulations: ICE6G-~~C~~

~~The ICE6G-C model~~We used the output data of the ICE6G_C (hereafter ICE6G) model as a basis for the extent of the major ice sheets at 1° resolution. ICE6G is a refinement of the ICE5G (VM2) model (Peltier, 2004) which has been widely used to model the distribution and dynamics of major ice ~~shields~~ sheets through time. The ICE6G-~~C~~ model explicitly ~~models~~ outputs changes in ice thickness of major ice sheets (e.g. the Laurentide ice sheet) from [the](#) Last Glacial Maximum (LGM) till today (Argus et al., 2014; Peltier et al., 2015) at 500 year time steps.

2.3 Observational glacial extent at Last Glacial Maximum (LGM)

105 As ~~the~~ extent of the glaciers during [the](#) LGM ([Last Glacial Maximum, hereafter defined as 21k BP similar to Ehlers et al. 2011](#)), we use data from ~~Ehlers et al. (2011)~~ Ehlers et al. (2011) that presents an up-to-date, detailed overview of Quaternary glaciations all over the world, not only with ~~regard~~ regards to stratigraphy but also with ~~regard~~ regards to major glacial landforms and the extent of the respective ice sheets.

2.4 Observational current glacial extent: GLIMS

110 The GLIMS (Global Land Ice Measurements from Space) project (Raup et al., 2007) at the NSIDC (National Snow and Ice Data Center) provides data on global glacial extent and other information about glaciers including metadata on how those outlines were derived. Here we use this database to delineate the current extent of the glaciers at high resolution globally.

Formatted: Font color: Auto

2.5 Global Multi-resolution Terrain Elevation Data 2010 (GMTED2010)

115 [The Global Multi-resolution Terrain Elevation Data 2010 \(GMTED2010\) \(Danielson and Gesch, 2011\) dataset contains elevation data for the globe collected from various sources. Here we use the 30-arc sec. version of the data that represents the mean elevation of all 7.5-arc sec. grid cells that represent the highest available resolution of the data.](#)

2.6 Bathymetric DEM

120 [We use the General Bathymetric Chart of the Oceans \(GEBCO\) 2014 \(Weatherall et al., 2015\) as bathymetry. Although GEBCO also includes land surface altitude, we only use it for the oceans, and we keep as land altimetric data that of the CHELSA V1.2 procedure to maintain comparable topography at the land surface.](#)

2.7 Global sea-level change

125 We used data from Miller et al. (2005) for the estimation of global sea-level change from 21k BP to 1990. The data provide
global estimates of sea level change over the last 100 million years. The entire time series of sea-level change is based on a
variety of proxy data, with the data used here, dating back to the LGM, being mainly based on tropical reef proxies (Miller et
al., 2005).

3 Methods;

130 Downscaling is based on ~~a derived version of the~~ CHELSA V1.2 ~~algorithm~~mechanistic downscaling model (Karger et al.,
2017a) ~~and forcings from CCSM3 TraCE 21k (He, 2011; Liu et al., 2009) and involved four main steps. (1) To apply the~~
~~CHELSA algorithm on the TraCE 21k data, we first approximated the paleo-orography using a combination of data from the~~
~~digital elevation model GMTED2010 (Danielson and Gesch, 2011), large scale ice sheet configurations from ICE6G (Peltier~~
~~et al., 2015), high resolution glacier extents from GLIMS (Raup et al., 2007) and (Ehlers et al., 2011), as well as sea level~~
135 ~~change data from (Miller et al., 2005). Subsequently, we coupled the paleo-orography with (2) temperature and (3)~~
~~precipitation, and (4) validated the resulting climatology.~~
~~using forcing from TraCE-21k simulations (Liu et al., 2009; He, 2011) and involving several processing steps (Fig. 1). The~~
~~CHELSA downscaling model needs a dynamic forcing in the form of GCM output (Karger et al., 2020) or gridded reanalysis~~
~~data (Karger et al., 2017a, 2021b), as well as a surface orography (i.e. topography above sea level) to run a suite of downscaling~~
140 ~~algorithms for key climatic variables such as air temperature and precipitation. As the orography at different time steps between~~
~~21k BP and current times is not available, we approximated it using a combination of data from the digital elevation model~~
~~GMTED2010 (Danielson and Gesch, 2011), large scale ice sheet configurations from ICE6G (Peltier et al., 2015), high~~
~~resolution glacier extents from GLIMS for current conditions (Raup et al., 2007) and LGM conditions (Ehlers et al., 2011), as~~
~~well as sea level change data from Miller et al. (2005) (Fig. 1). We then ran the CHELSA V1.2 model on the paleo-orography~~
145 ~~using a bias corrected version of the TraCE-21k simulations as forcing. Details on these steps are described in the following~~
~~sub sections.~~

Formatted: Font: 11 pt

Formatted: Font: 11 pt, Not Bold

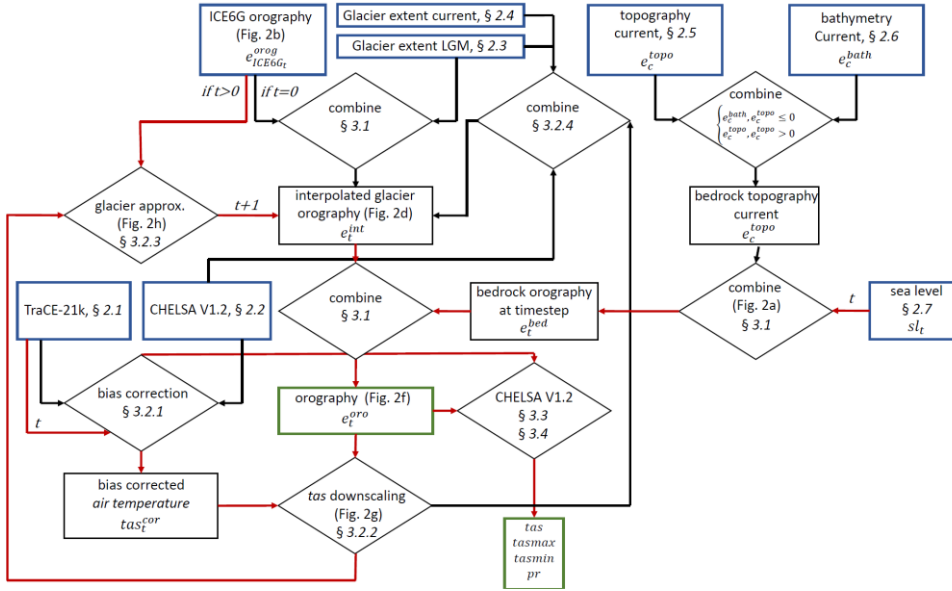


Fig. 1. Graphical representation of the different steps employed in downscaling TraCE-21k simulations using the CHELSA V1.2 model. Input datasets are indicated by blue box, output data are indicated by a green box. Rhombi indicate processing steps. t indicates discrete timesteps, with $t=0$ being the LGM. Red lines indicate processing steps that are run iteratively over all time steps, black lines indicate computations that were run only once.

3.1 Paleo-orography

The first step in estimating the downscaling paleo-orography was to combine annual-mean temperature data with sea-level data for the LGM (21k BP). For this time point, both estimates of glacial extents from Ehlers et al., 2011 and estimates of glacier thickness from ICE6G exist. We first combined the topographic information from GMTED2010 on land, and that of GEBCO into a bedrock topography that provides the surface elevation and ICE6G data to estimate combined ice + e. To create a bedrock orography e_t^{bed} (i.e. topography adjusted for sea level without glaciers), we used the information on past sea-level changes and set all elevations to 0 so that:

$$e_t^{bed} = e_c^{topo} - sl_t \quad (1)$$

To include the orography of the glaciers we first converted the polygons of the glacial extents from Ehlers et al. 2011 into point locations (Fig. 2a, black dots), and extracted their elevation from e_t^{bed} (Fig. 2a) at time $t=0$ (LGM, 21k BP) resulting in the surface orography. The rationale behind this approach is that temperature and glacier extents are to some degree interdependent, and a change in temperature will translate to a change in glacial extent. This approach was implemented by first combining the elevation of the glacial boundaries (gb) $e_{gb_t}^{bed}$. To combine the high-resolution glacial extents from (Ehlers et al., 2011) with the estimates from Ehlers et al. (2011), with the coarser (1°) resolution of ICE6G data. To do so, we randomly sampled 100 point locations per 1° grid cell from ICE6G and again extracted the height of the glacier plus the surface elevation e_t^{ice} at time 0 (LGM) of the glaciers from e_t^{bed} at the ICE6G timestep that is nearest to the timestep $t=0$ (LGM, 21k BP) resulting in e_{G_t} (Fig. 2b). All points that did not fall within the high-resolution glacial extent were omitted. We then converted the polygons of the glacial extents into point locations as well, and extracted their elevation e_{G_t} from the DEM at time e_t^{dem} , where $e_t^{dem} = e^{dem} - e_s$ with e_s being the difference between the current and past sea surface elevation at time t , so that only point within the high-resolution estimate of glacial extent from Ehlers et al. (2011) remained (Fig. 2b). Then both point datasets $e_{gb_t}^{bed}$ and $e_{ICE6G_t}^{orog}$ were combined to e_t^{obs} containing represent a point sample of the surface orography. This elevation e_{G_t} within the high-resolution glacial extent of Ehlers et al. (2011) (Fig. 2c). Next, this point sample was then spatially interpolated to a grid of 30 arc sec resolution applying multilevel B-spline interpolation-interpolations. By this, we achieved an interpolated gap free high-resolution estimate of glacial surface elevation e_t^{int} at $t=0$ (LGM, 21k BP) (Fig. 2d). The multilevel B-splines use a B-spline approximation to $e_t e_{G_t}$ and starts start using the coarsest grid ϕ_0 from an overall set of grids $\phi_0, \phi_1, \dots, \phi_n$ with $n = 14$ generated using optimized B-spline refinements (Lee et al., 1997). The resulting B-spline function $f_0(e_t^{obs})e_{G_t}$ then gives the first approximation of $e_t e_t^{int} \equiv f_0(e_t)e_{G_t}$ and leaves a deviation:

$$\Delta^1 e_t^{obs} = e_t^{obs} e_t^{int} = e_t^{int} - f_0(x_c, y_c)$$

(12)

Formatted: Tab stops: 17 cm, Right

at each grid cell c location $(x_e, y_e, e_e^{obs}) \rightarrow (x_c, y_c, e_c^{int})$. Then the next control lattice ϕ_1 is used to approximate $f_1(\Delta^1 e_e^{obs} e_c^{int})$. This approximation is then repeated on the sum of:

$$f_0 + f_1 = e_e^{obs} e_c^{int} - f_0(x_c, y_c) - f_1(x_c, y_c)$$

(2)

at each pointgrid cell c $(x_e, y_e, e_e^{obs}) \rightarrow (x_c, y_c, e_c^{int})$ n times resulting, in our case, in the gap free interpolated glacial surface e_c^{int} . The interpolated glacial surface was then combined with e_{DEM}^{bed} to the orographytopography $e_e^{oro} e_t$ (Fig. 2e) using:

$$e_e^{oro} = \{ e_e^{dem}, e_e^{dem} \geq e_c^{int} e_c^{int}, otherwise \} \quad (3)$$

3.2 Temperature coupling

$$e_t = \begin{cases} e_t^{topo}, & e_t^{topo} \geq e_t^{int} \\ e_t^{int}, & otherwise \end{cases} \quad (4)$$

The estimatedfinal orography at the LGM e_t^{oro} at timestep $t=0$ (i.e. topography above sea level) (Fig. 2f) is then generated using:

$$e_t^{oro} = \begin{cases} 0, & e_t \leq sl_t \\ e_t, & e_t > sl_t \end{cases} \quad (5)$$

With sl_t being the sea-level at timestep t . Although this approach includes changes in the glacial surface and sea-level rise, it ignores changes in bedrock elevation due to upwelling after glacier melt.

Formatted: Tab stops: 17 cm, Right

3.2 Interpolation of glacier extent and thickness between LGM and current

As high-resolution estimates of glacial surface elevation are not available for timesteps t other than the LGM and current, we use a combination of mean annual 2m air temperature data, together with sea surface elevation sl_t and ICE6G orography $e_{ICE6G_t}^{oro}$ data to estimate e_t^{oro} at each time step $t \neq 0$. The rationale behind this approach is that temperature and glacier extents are interdependent, and a change in temperature will translate into a change in glacial extent or thickness. The procedure to generate high resolution glacial surfaces is explained in the following sections.

3.2.1. Bias correction of air temperature

In a first step, the orography e_t^{oro} with $t=0$ (LGM, 21k BP) was then used to downscale mean annual temperature $tas_t = tas_t$. GCMs such as the CCSM3 normally exhibit a large bias in temperatures or precipitation (Cannon et al., 2015; Maraun, 2013). We therefore applied a change factor bias correction based on the bias observed between current annual mean annual 2m air temperatures tas_{cur}^{obs} from CHELSA V1.2 resampled to a 0.5° grid resolution, where the and that of TraCE21k simulated for the same time period tas_{cur}^{mod} spline interpolated using same multilevel B-spline interpolation method as described in 3.1 to the 0.5° grid resolution. We used the time period 1980-1990 ($=cur$) to calculate this bias, as it is the only time period for which CHELSA V1.2 and TraCE21k overlap. The change factor was then calculated from the $\Delta tas = tas_{cur}^{mod} - tas_t^{mod}$ as:

$$\Delta tas = tas_{cur}^{obs} - tas_{cur}^{mod} \quad (6)$$

This effectively preserves the trends observed in temperature, but simultaneously assumes that the bias has also been conserved over time (Maraun, 2016). For the interpolation of Δtas to the 0.5° grid resolution of tas_{cur}^{obs} the same multilevel B-spline interpolation was used as described above. The bias corrected temperatures tas_t^{cor} are then given by:

$$tas_t^{cor} = tas_{cur}^{obs} - \Delta tas \quad (7)$$

3.2.2. Downscaling mean annual air temperature

To achieve a high-resolution temperature approximation of near surface air temperatures (Fig. 2g), we used a lapse rate-based downscaling from atmospheric temperature data at the TraCE-21k pressure levels. The lapse rates Γ are based on a linear approximation from average temperatures ta_z at altitudes a_z at vertical levels 26 (992.5 hPa) to 20 (600.5 hPa) of the T31_gx3v5 grid that contain all surface elevations so that:

$$\Gamma = \frac{n(\sum a_z ta_z) - (\sum a_z)(\sum ta_z)}{n(\sum a_z^2) - (\sum a_z)^2}$$

Formatted: Tab stops: 17 cm, Right

255

260

(4)(8)

Temperature at the surface at a high spatial resolution tas was then calculated by:

265

$$tas_t = I_t * e_t^{oro} + tas_t^{cor}$$

270

(5)(9)

275

To couple the outline of the glacier to the **3.2.3. Glacier extent approximation using mean annual air temperature** We assume that air temperature is correlated to glacier extent and use this relationship to estimate the boundaries of glaciers for each time step separately. To do so, we use mean annual 2m air temperature at the boundary of the interpolated high-resolution glacier orography. We then transformed the glacier elevations $e_t^G = e_t^{dem} \leftarrow e_t^{int} e_t^{int}$, to a polygon, G_{t_1} and then transformed the outline of this polygon to a point sampling of the glacier boundaries at time t : e_t^{GB} . Temperatures $tas_t^{GB} = 0$. Mean annual 2m air temperatures at this glacier boundary were then extracted for each boundary location coordinate (x, y) during the LGM ($t = 0$) this point sample which gives the local annual mean air temperature $tas_{t=0}^{gb}$ under which a glacial boundary existed during the LGM $(x_{tas_0^{gb}}, y_{tas_0^{gb}})$. As this simple coupling between glacial boundaries and annual temperatures is however only glacier had a rough estimate, we additionally included boundary at the LGM. To set this in relation to current mean annual air temperatures and at current glacier boundaries $tas_{t=221}^{gb}$ (with $t=221$ being the year 1990).

285

Formatted: Tab stops: 17 cm, Right

Formatted: Font: Bold

Formatted: Font: Bold

Formatted: Font: Bold

we calculated the difference between current and LGM boundary temperatures. Here, the locations for the current glacial boundaries were extracted $\left(x_{tas_{cur}^{gb}}, y_{tas_{cur}^{gb}}\right)$ and locations of current and LGM glacial boundary temperatures were combined. The resulting point locations for both $tas_{t=0}^{gb}$ and $tas_{t=221}^{gb}$ were then spatially interpolated using a multilevel-B-spline (as described in 3.1) to result in a gap-free surface and then subtracted resulting in Δtas_{cur}^{obs} (Fig. 2g).

As the orography for the next time step is not known yet, we estimated the near surface air temperature tas_{t+1}^{est} for the glacial melt reduction in glacier extent similar the orography from the time step before. So that:

$$tas_{t+1}^{est} = \Gamma_{t+1} * e_t^{oro} + tas_{t+1}^{cor}$$

(6)(10)

The binary glacial extent G_{t+1} at $t + 1$ is then approximated as:

$$G_{t+1} = \begin{cases} 1, & tas_{t+1}^{est} < tas_t^{GB} + \frac{\Delta tas_{cur}^{obs}}{-1 * (\sum t-t)} \wedge G_0 = 1 \\ 0, & otherwise \end{cases}$$

(7)(11)

This glacial extent is then used again to estimate the combined topography at $t+1$ in the same way as described in 3.1. As ICE6G has a 500 year resolution we used the ICE6G orography used that is closest to each timestep. As ICE6G only includes information on the major ice sheets, smaller ice sheets in the Alps do not include a sample of $e_{ICE6G_t}^{oro}$. In the case of smaller

ice sheets, the surface orography from ICE6G is replaced by a point sample of the elevation of the glacier boundary under current conditions $e_{gb_c}^{orog}$ (Fig. 2h). The glacier orography in this case is then created by using a spline interpolation between

$e_{gb_t}^{bed}$ and $e_{gb_c}^{orog}$. In Eq. 11 the second term in the condition for G_{t+1} linearly scales $\Delta t a s_{cur}^{obs}$ over the entire number of time steps. This correction is necessary, as otherwise the entire bias would be added at the first time step, resulting in an unrealistically strong shift in the glacial extent. We then repeated the transformation of the glacial extent G_{t+1} to all point locations and repeated the procedure for the temperature coupling to estimate the orography e_{t+1}^{orog} . Near surface air temperatures for $t + 1$ have been then approximated using:

$$tas_{t+1} = T_{t+1} * e_{t+1}^{orog} + tas_{t+1}^{cor}$$

Formatted: Tab stops: 17 cm, Right

3.3 Precipitation estimation

3.3 Downscaling mean monthly precipitation rates

3.3.1 Orographic wind effects

The estimation of high-resolution precipitation follows a variant of the CHELSA V1.2 algorithm (Karger et al. 2017). The CHELSA V1.2 algorithm assumes elevation to be the main driver of vertical precipitation gradients, which is however, highly idiosyncratic (Basist et al., 1994; Böhner, 2006; Böhner and Antonic, 2009; Daly et al., 1997; Gao et al., 2006; Karger et al., 2017a; Sevruk, 1997; Spreen, 1947). (Spreen, 1947; Basist et al., 1994; Daly et al., 1997; Sevruk, 1997; Böhner, 2006; Gao et al., 2006; Böhner and Antonic, 2009; Karger et al., 2017a). In tropical convective regimes, precipitation typically increase up to the condensation level around 1000-1500 m above surface, while the exponentially decreasing moisture content in the mid-to upper troposphere results in a drying above the condensation level resulting in non-linear precipitation lapse rates (Körner, 2007). Furthermore, negative precipitation lapse rates are common under the extremely dry polar climates. In contrast, at mid-latitudes and in the subtropics, precipitation generally increases with increasing elevation due to advection. As a consequence, summits of the Alps or other high mountain ranges exhibit high rainfall (Rotunno and Houze, 2007), and lapse

350 rates for precipitation are almost linear (Weischet and Endlicher, 2008). To approximate the effects of orographic precipitation we used [a variant of the CHELSA V1.2 algorithm](#), which is explained in [more](#) detail below. We used 10 m u -wind and v -wind [components](#) of TraCE-21k to calculate wind direction. Both wind components were projected to a world Mercator projection [and then interpolated to a](#) 4 km grid resolution using a multilevel B-spline interpolation similar to the one [used for the bias correction surface described in 3.1](#). Windward and leeward effects are assumed to be best represented at resolutions larger than [4 km](#) (Daly *et al.*, 1994), we therefore chose a grid resolution of [4 km](#) for the underlying digital elevation model. The wind effect H was then calculated using:

$$H_W = \frac{\sum_{i=1}^n \frac{1}{d_{WHi}} \tan^{-1} \left(\frac{d_{WZi}}{d_{WHi}^{0.5}} \right)}{\sum_{i=1}^n \frac{1}{d_{LHi}}} + \frac{\sum_{i=1}^n \frac{1}{d_{LHi}} \tan^{-1} \left(\frac{d_{LZi}}{d_{LHi}^{0.5}} \right)}{\sum_{i=1}^n \frac{1}{d_{LHi}}} \quad (9)$$

360

365

Formatted: Tab stops: 17 cm, Right

$$H_L = \frac{\sum_{i=1}^n \frac{1}{\ln(d_{WHi})} \tan^{-1} \left(\frac{d_{LZi}}{d_{WHi}^{0.5}} \right)}{\sum_{i=1}^n \frac{1}{\ln(d_{LHi})}} \quad (10)$$

370

375

Formatted: Tab stops: 17 cm, Right

380 where d_{WHi} and d_{LHi} refer to the horizontal distances between the focal [4 km](#) grid cell in windward and leeward direction and d_{WZi} and d_{LZi} are the corresponding vertical distances compared with the focal [4 km](#) cell following the wind trajectory. The second summand in the equation for H_W where $d_{LHi} < 0$ accounts for the leeward impact of previously traversed mountain chains. The horizontal distances in the equation for H_L where $d_{LHi} \geq 0$ lead to a longer-distance impact of leeward rain shadow. The final wind-effect parameter is calculated as $H = H_L H_W$. Both equations were applied to each grid cell at the 30-arc sec. resolution in a World Mercator projection. Orographic precipitation effects are less pronounced just

385

above the surface, as well as in the free atmosphere above the planetary boundary layer (Daly et al., 1997; Karger et al., 2020; Oke, 2002; Stull, 2012). (Daly et al., 1997; Oke, 2002; Stull, 2012; Karger et al., 2020). The highest impact of orography is considered just at the boundary layer height where the airflow interacts with the terrain. We used the lifted condensation level (LCL) as indicator of the altitude at which the wind effect exerts the highest contribution to precipitation. The LCL has been calculated using the mean air temperature (*tas*) and mean *near surface* relative humidity (*RH_{hurs}*) using:

Formatted: Font: Italic

$$LCL = 20 + (tas/5) * (100 - RH_{hurs})$$

Formatted: Tab stops: 17 cm, Right

(Lawrence, 2005). The LCL has been interpolated to the CHELSA resolution using a B-spline interpolation. To create a boundary layer height corrected wind effect *H_B*. The wind effect grid *H* containing *LCL* was then proportionally distributed to all grid cells falling within a respective T31 grid cell using:

Formatted: Tab stops: 17 cm, Right

$$H_B = \frac{H}{1 + \left(\frac{LCL - H_{min}}{H_{max} - H_{min}} \right)}$$

(12)

$$\frac{H}{1 - \left(\frac{|z - LCL_z| - z_{max}}{h} \right)}$$

(16)

420

With z_{max} being the being the maximum distance between the lifted condensation level LCL_z at elevation z and all grid cells at a 30-arc sec. resolution falling within a respective T31 grid cell, h being a constant of 9000 m, and z being the respective elevation from GMTED2010 (Danielson and Gesch, 2011) with:

425

$$LCL_z = LCL + z_{GCM} + f$$

430

430

(13)

(17)

435

B being the height of the monthly means of daily mean boundary layer from TraCE21k, z_{GCM} being the elevation of the TraCE21k grid cell, and f being a constant of 500 m which takes into account that the level of highest precipitation is not necessarily at the lower bound of the LCL, but slightly higher (Karger et al., 2017a).

440

The wind effect algorithm cannot distinguish extremely isolated valleys inside highly-elevated mountain areas (Frei and Schär, 1998). Such valleys are situated in areas where the wet air masses flow over an orographic barrier and are prevented from flowing into deep valleys. These effects are mainly confined to large mountain ranges, and are not as prominent in small- to intermediate-sized mountain ranges (Liu et al., 2012). Such dry valleys are situated in areas where the wet air masses flow over an orographic barrier and are prevented from flowing into deep valleys (Karger et al., 2020). To account for these effects, we used a variant of the windward-leeward equations with a linear search distance of 300 km in steps of 5° from 0° to 355° circular for each grid cell. The calculated leeward index was then scaled towards higher elevations using:

Formatted: Tab stops: 17 cm, Right

15

$$E = \left(\frac{\sum_{i=1}^n \frac{1}{d_{WHi}} \tan^{-1} \left(\frac{d_{LZi}}{d_{WHi}} \right)^z}{\sum_{i=1}^n \frac{1}{d_{LHi}}} \right)^{\frac{1}{n}}$$

Formatted: Tab stops: 17 cm, Right

(14)(18)

c was set to 9000 m^{-2} , h has been set to 9000 m. $E * H_B$ will give the first approximation of the orographic precipitation intensity p_I .

3.3.2. Bias correcting precipitation and downscaling

Precipitation, similar to temperature exhibits a rather large bias in TraCE-21k (Fig. 3, Fig. 4). To remove this bias, we applied a change factor bias correction similar to the one described in 3.2.1. Here, we used a multiplicative change factor, to avoid precipitation rates < 0 . Additionally, we included a constant of $c = 0.0001 \text{ kg} \cdot \text{m}^{-2} \cdot \text{month}^{-1}$, to avoid division by zero so that:

$$\Delta p r_m = (p r_{curm}^{mod} + c) / (p r_{curm}^{obs} + c) \quad (19)$$

with m being the respective month of the year. The bias corrected precipitation rate for p_m^{cor} is then calculated by:

$$p r_m^{cor} = p r_{curm}^{obs} / \Delta p r_m \quad (20)$$

To achieve the distribution of monthly precipitation $p r_o$ given the approximated orographic precipitation intensity p_{Ic} at each grid location (x_c, y_c) , we used a linear relationship between $p_m^{cor} p r_m^{cor}$ and $p_{Ic} p r_{Ic}$ using:

$$p r_o = \frac{p_{Ic}}{\frac{1}{n} \sum_{i=1}^n p_{Ici}} * p_m^{cor} p r_m^{cor}$$

Formatted: Tab stops: 17 cm, Right

480

485

(15)(21)

where n equals the number of 30-arc sec. grid cells of p_i that fall within a 0.255 grid cell of p_m^{cor} .

490

3.4. Downscaling mean monthly near surface air temperatures

The downscaling of monthly near surface air temperatures (tas , $tasmax$, $tasmin$) follows the methods described in 3.2.2., with the only difference that instead of mean annual temperature, $tasmax$ and $tasmin$ are used, where $tas = (tasmax + tasmin)/2$. The temperatures have again first been bias corrected using:

495

$$\Delta tas_m = tas_{cur_m}^{obs} - tas_{cur_m}^{mod} \quad (22)$$

and:

500

$$tas_{m_t}^{cor} = tas_{cur_m}^{obs} - \Delta tas_m \quad (23)$$

with m being the respective month of the year, and tas being interchangeable for $tasmax$ and $tasmin$ in Eq. 22 and Eq. 23.

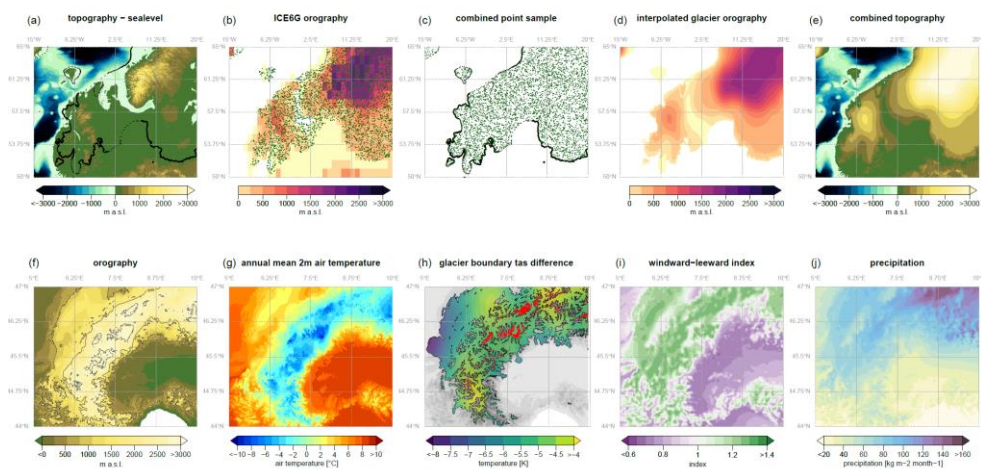


Figure 2. Illustration of several steps performed to estimate the surface orography and the temperature and precipitation fields in CHELSA-TraCE21k during the last glacial maximum (21k BP). The upper row gives an example of the interpolation of the European ice sheets, the lower row shows an example of the resulting orography and environmental variables in the western part of the European Alps. **a)** Topographic information at $t=0$ (LGM) is combined with information on past sea-levels and the boundary of ice sheets (black dots) for which the surface elevation is extracted. **b)** Within the extent of ice sheets, surface elevation is extracted from the ICE6G orography for a random sample of points for $t=0$. **c)** Both point samples from **a)** and **b)** are combined and interpolated **d)** to estimate the orography of the glaciers. **e)** The interpolated glacier orography and the sea-level adjusted topography **a)** are then combined. **f)** The high resolution (30 -arc sec) orography (shown here for the western Alps) is then used as basis at $t=0$ for **g)** a lapse-rate based downscaling of air temperature. **h)** From the high-resolution temperatures information on the glacier boundaries during the LGM (black) and current times (red) is extracted and the difference is interpolated to correct the temperature based shrinking and expansion of the glaciers. **i)** based on the orography the windward-leeward index is calculated (shown for July 21k BP), that builds the basis for the **j)** precipitation approximation.

Formatted: Line spacing: Multiple 1.15 li

Formatted: Font: Not Bold

4 Output validation

Direct validation of the temperature (Fig. 1) and precipitation (Fig. 2) output at high resolution for paleo time series generally relies on proxies, as direct observations of both variables are not available. Although global temperature time series exist, they only give global means, and do not allow validation of the performance of a 4km1-km paleo climatic dataset. Therefore, to validate the CHELSA_TraCE21k dataset we complement a simple comparison of the simulated time series to proxy data and

current observations, with approaches of validating derived parameters from the simulated temperature and precipitation that directly benefit from a very high horizontal resolution.

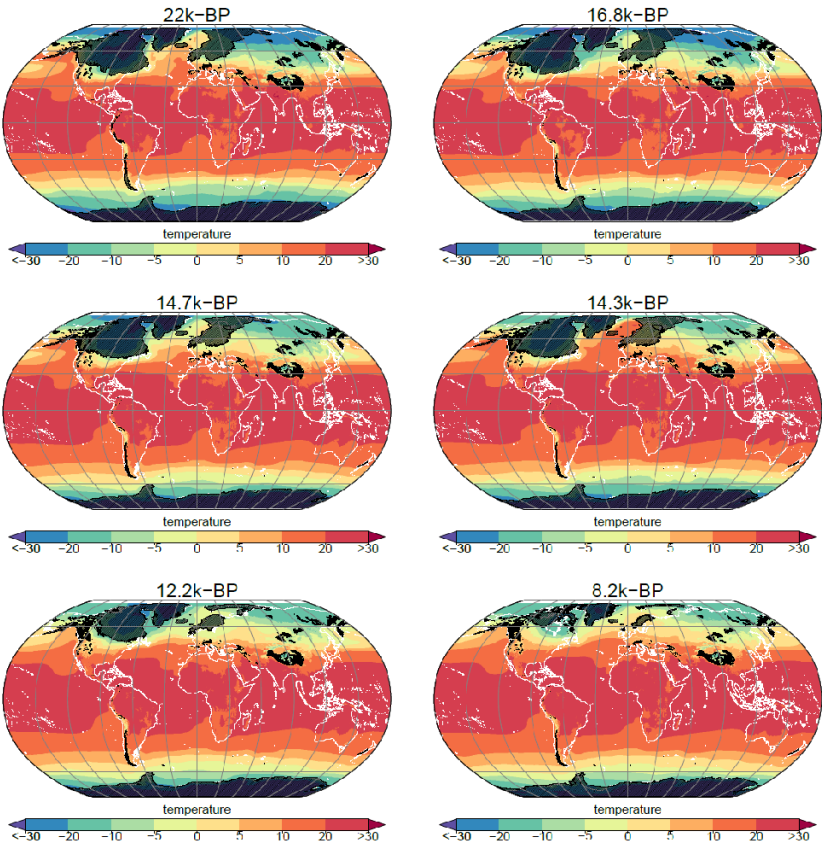


Figure 1: Mean annual near surface air temperature for time periods before present (BP) that showed exceptional climate dynamics in the northern Atlantic region, from the CHELSA_TrACE21k model. The interpolated extent of the glaciers at each time step is shown as shaded black polygons. The approximated coast lines are delineated in white. The last glacial maximum is shown for 22k-BP. The Heinrich I event, during which the northern Atlantic was actually colder compared to the LGM, is shown in 16.6k-BP. The extreme warming at the Bølling-Allerød is evident from the comparison of 14.7k-BP, shortly before the onset, and 14.3k-BP, the maximum of the Bølling-Allerød warming. The middle of the Younger Dryas cold period is shown at 12.2k-BP. The 8.2 kiloyear event is shown at 8.2k-BP.

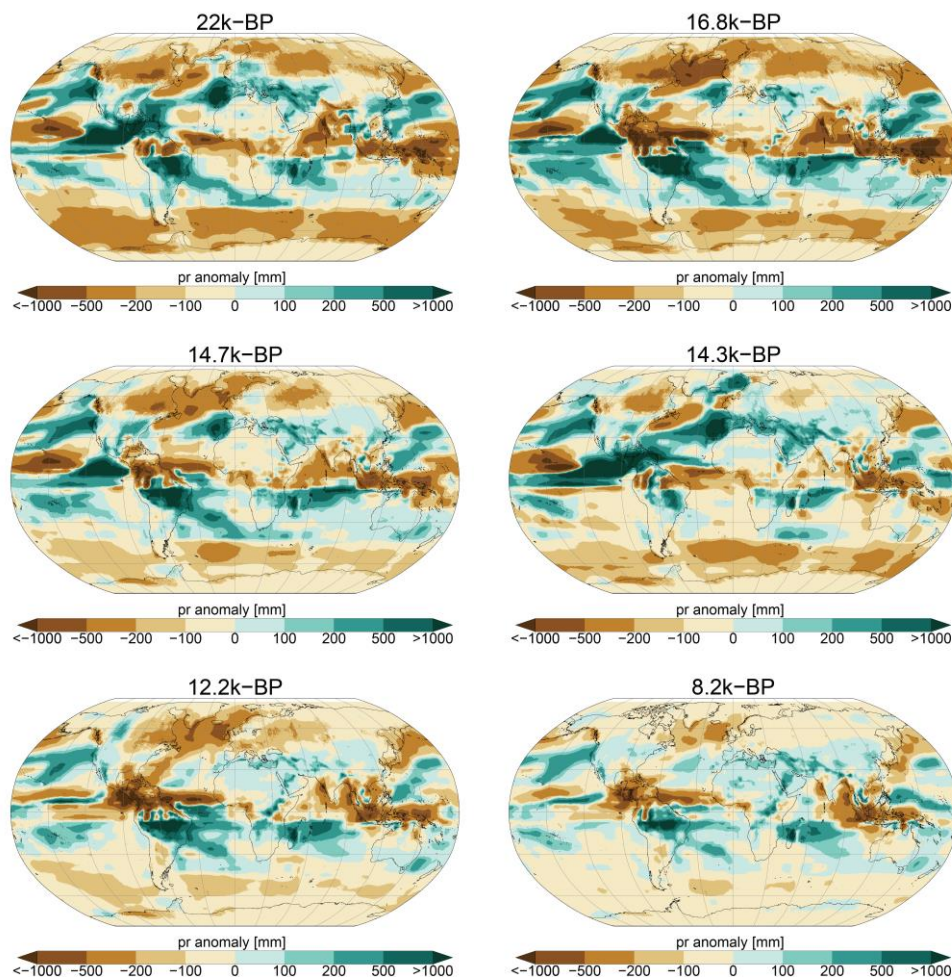


Figure 2: Anomalies in annual precipitation sums from the precipitation of the 1990 period for time periods before present (BP) that showed exceptional climate dynamics, from the CHELSA_TrACE21k model. The approximated coast lines are delineated in black. The last glacial maximum is shown for 22k-BP. The Heinrich I event, during which the northern Atlantic was actually colder and dryer compared to the LGM, is shown in 16.6k-BP. The extreme warming at the Bølling-Allerød with increased precipitation is evident from the comparison of 14.7k-BP, shortly before the onset, and 14.3k-BP, the maximum of the Bølling-Allerød warming. The middle of the Younger Dryas, a cold period with lower precipitation in the northern Atlantic region, is shown at 12.2k-BP. The 8.2 kiloyear event is shown at 8.2k-BP. At this event, precipitation shows the lowest overall anomalies from current precipitation.

4.1 Validation using current (historical) observations

We used data from the Global Historical Climate Network (GHCN) monthly database V.3 (Lawrimore et al., 2011) to validate the performance of the downscaling algorithm during the last time step of the CHELSA-TraCE21k for which station data is available. To do so we calculated monthly climatologies for each month for *tasmax*, *tasmin*, and *pr* from both TraCE21k and CHELSA-TraCE21k. We then compared the values measured at each station to that simulated in both, TraCE21k and CHELSA-TraCE21k.

The original TraCE-21k data shows large deviations and root mean squared errors (RSME) from the observed data (Fig. 3). This is somewhat expected as a climate model running for such long time periods needs to have coarse resolution, as well as a large degree of generality and realism which decreases the accuracy of a model when compared to observations. The temperature variables perform well in TraCE-21k with $r \sim 0.8$ for all months, but have deviations and RSME similar to those of precipitation, that most likely can be attributed to the coarse resolution of the climate model. TraCE-21k also seems to overestimate temperature extremes both for *tasmax* and *tasmin* (Fig. 4).

The precipitation however, does not perform well in the model with $r \sim 0.4$ and large deviations from actual values (Fig. 3) and overall precipitation seems to be too low in the model (Fig. 4).

The CHELSA downscaling algorithm improves the correlation between observed and modelled data and decreases the standard deviation for all three parameters (Fig. 3). The downscaling for the temperature variables increases the correlation to $r \sim 0.95$ for all months and decreases the standard deviation substantially (Fig. 3). Similarly, the performance of the precipitation estimation in CHELSA-TraCE21k increases, which is reflected in a $r \sim 0.7$ and a lower standard deviation and RSME (Fig. 3). The underestimation of precipitation in the TraCE21k is reduced, but the downscaling algorithm still has a considerable bias (Fig. 3) during the historical period.

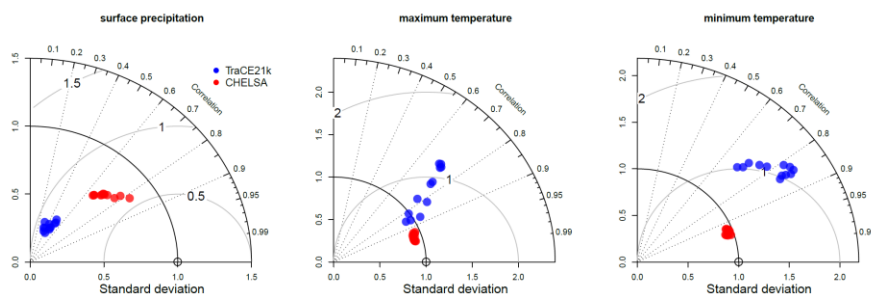


Figure 3: Taylor diagrams comparing the relationship between TraCE-21k (blue) and CHELSA-TraCE21k (red). Data is shown for the 20th century time period with average monthly observational data from the Global Historical Climate Network (GHCN) for the time period 1950-1990. Each dot represents a specific month.

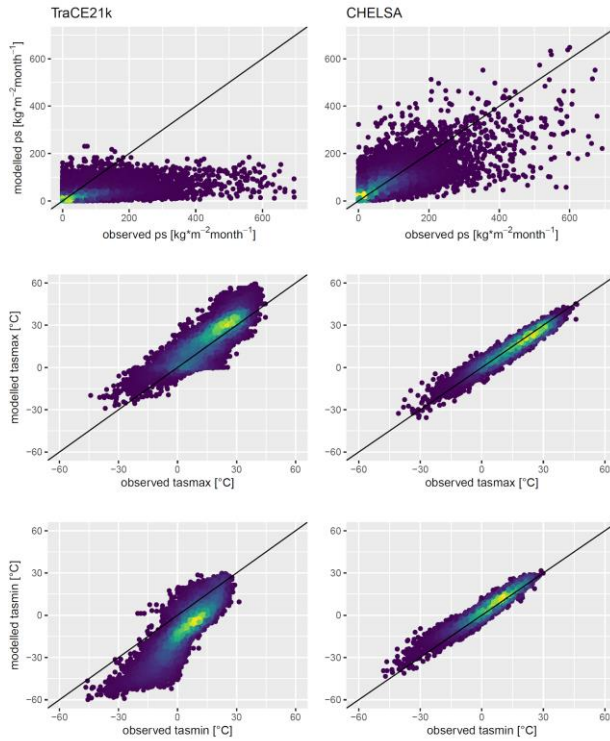


Figure 4: Scatter plots comparing precipitation, maximum-, and minimum temperature. Although the downscaling algorithm might increase the performance of the temperature and precipitation estimates during the historical period, this does not imply that this improvement is equal during the entire transient time series. To further validate the data, we therefore compared it to more derived parameters for which time series data exists.

Data are aggregated from TraCE-21k and CHLSA-TraCE21k for the 20th century time period with observational data from the Global Historical Climate Network (GHCN) for the time period 1980-1990.

4.2 Comparison with temperature proxies from ice core data

We compared the downscaled temperatures with the Greenland ice core reconstructions of Buizert et al. (Buizert et al., 2014, 2018) to check the performance of the downscaling at eight ice core locations on the Greenland Ice Sheet (GIS).

Although both temperature reconstructions and GCM generated temperatures have uncertainties connected to them (Erb et al., 2018), the ice core data are so far the best possible validation dataset that spans the entire deglaciation period from 24kBP to 1990 (Buizert et al., 2014, 2018). To assess the performance gain of the downscaling over the coarse resolution TraCE21k data, we compare the ice core annual mean near surface temperature reconstructions with both the CHELSA-TraCE21k, and the original TraCE21k temperature data.

Compared to the temperature reconstructions from ice cores, the downscaled CHELSA-TraCE21k model had reduced bias at four of the ice core sites located at the edges of the GIS (ReCAP, Agassiz, Hans Tausen Iskappe, Camp Century), but increased the bias, RMSE and MAE at the remaining four sites at the center of the GIS (NEEM, NGRIP, GISP2, Dye 3) (Fig. 5). Overall, both CHELSA-TraCE21k as well as TraCE21k show a warm bias before the Heinrich 1 event (i.e. the break off of large groups of icebergs from Greenland into the North Atlantic, 16.8k BP), and roughly after the 8.2k event at four of the sites (ReCAP, Agassiz, Hans Tausen Iskappe, Camp Century). At three sites (ReCAP, Agassiz, Hans Tausen Iskappe, Camp Century) a cold bias is present after the younger Dryas (Fig. 5). At the four other sites, CHELSA-TraCE21k usually shows a warm bias before the H1, and TraCE-21k a cold bias before the H1 (Fig. 5). After the younger dryas (12.9k BP – 11.6k BP), both models show a cold bias at these sites. At the Camp Century site, the Trace data are close to the $\delta^{15}\text{N}$ -based temperature reconstructions before the H1 event, and CHELSA-TraCE21k shows a warm bias, while after the younger dryas the situation is reversed (Fig.

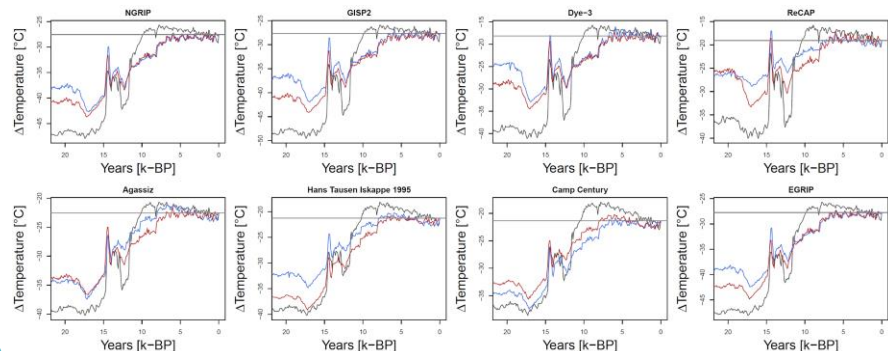


Figure 5: Comparison of temperature anomalies from current (1950-1990) for the CHELSA-TraCE21k time series data (blue), the TraCE21k data (red), and the temperature reconstructions from ice cores (black) for 8 sites across Greenland. The grey horizontal line indicates the current observed temperature during the period 1981-2010 from CHELSA V2.1. Temperatures are plotted as anomalies from the current temperature recorded at the respective location of the ice cores.

The bias observed after downscaling might be related to factors to a bias in all the different input sources, such as the TraCE-21k bias being amplified, a bias in the ice-core proxy data itself, or the bias correction using the relatively simple change factor

600 method. With the available data, these potential causes cannot clearly be disentangled, but should be kept in mind for applications of the data.

4.3 Validation of glacier extent between 18kBP-18k BP and 14kBP-1k BP

605 Although the downscaling algorithm might increase the performance of the temperature and precipitation estimates during the historical period, this does not imply that this improvement is equal during the entire transient time series. To further validate the data, we therefore compared it to more derived parameters for which time series data exists.

As the ice core temperature reconstructions have associated uncertainties, it is impossible to disentangle if potential differences between the ice core data and the model data are due to uncertainties in the reconstructions. To validate the downscaled temperature data further, we used the interpolated extent of glaciers in CHELSA-TraCE21k, and compared it to glacial extent data from Dyke et al. 2003. The data consists of expert delineated glacier maps based on a chronological database of radiocarbon dates and contains >4000 dates located in North America (Dyke et al., 2003). To compare both datasets, we first calculated the glacial extent from CHELSA-TraCE21k by assigning each 1km grid cell in a Lambert Conformal Conic projection (+proj=lecc+latso that each data point compared equals 1=49+lat_2=77+lat_0=49+lon_0=95+x_0=0+y_0=0+ellps=chrk66+units=m+no_defs, extent=x_min:-3698534, x_max:-3596392, y_min:-1259083, y_max:-4674296) to km² either to 615 being covered by a glacier [1] or being free of glacier [0]. We assigned a 1 if the simulated glacier height was above the paleo terrain elevation, and a 0 if it was lower or equal to the paleo terrain elevation. The paleo terrain elevation was calculated using the current terrain elevation minus the sea level difference between current and that of the respective paleo timestep. As the current terrain elevation already includes extent glaciers, this elevation dependent procedure of assigning glacial extents would result in the current glaciers being assigned a 0. Therefore, we assigned all grid cells covered by extent glaciers a 1.

620 To compare the simulated glacial extent to the expert delineated extent, we rasterized the polygons provided by Dyke et al., 2003 for the years 18 kBP - 1 kBP 18k BP - 1k BP to the 1km resolution, extent, and projection of the simulated glacial cover and assign a 1 where the polygon intersects with a 1km raster cell and a 0 otherwise.

We then calculated three different test values to identify if the simulations correctly predict the presence and absence of a glacier. As the dataset is highly unbalanced between absences of glaciers [0] and presences of glaciers [1] through time we use balanced accuracy which is defined as: (sensitivity+ specificity)/2. Additionally we report Cohen's Kappa, and the True Skill Statistic (Allouche et al., 2006).

5 Validation results

5.1 Accuracy of temperature and precipitation estimated during the current (historical) period

630 The original TraCE21k data shows large deviations and root mean squared errors (RSME) from the observed data (Fig. 3). This is somewhat expected as a climate model running for such long time periods needs to have coarse resolution, as well as

Formatted: Font: Italic

Formatted: Font: Italic

Formatted: Font: Not Bold

a large degree of generalism and realism which decreases the accuracy of a model when compared to observations. The temperature variables perform well in TraCE21k with $r \sim 0.8$ for all months, but have deviations and RSME similar to those of precipitation, that most likely can be attributed to the coarse resolution of the climate model. Trace21k also seems to overestimate temperature extremes both for *tasmax* and *tasmin* (Fig. 4).

The precipitation however, does not perform well in the model with $r \sim 0.4$ and large deviations from actual values (Fig. 3) and overall precipitation seems to be too low in the model (Fig. 4).

The downscaling algorithm improves the correlation between observed and modelled and decreases the standard deviation for all three parameters (Fig. 3). The downscaling for the temperature variables increases the correlation to $r \sim 0.95$ for all months and decreases the standard deviation substantially (Fig. 3). Similarly the performance of the precipitation estimation in CHELSA-TraCE21k increases, which is reflected in a $r \sim 0.7$ and a lower standard deviation and RSME (Fig. 3). The underestimation of precipitation in the TraCE21k is reduced, but the downscaling algorithm still has a considerable bias (Fig. 3) during the historical period:

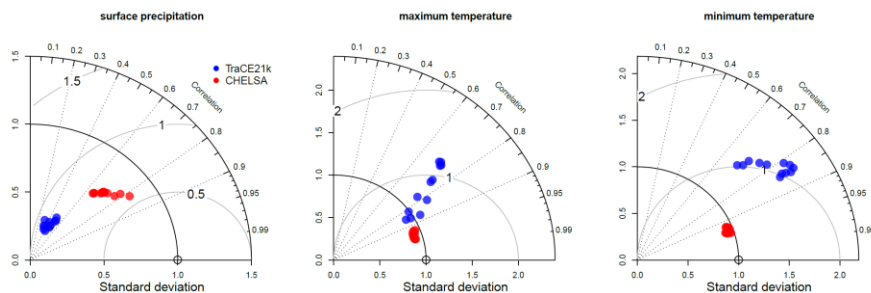


Figure 3: Taylor plots comparing the relationship between fCCSM3-TraCE21k (blue) and CHELSA-TraCE21k (red). Data is shown for the 20th-century time period with observational data from the Global Historical Climate Network (GHCN) for the time period 1950–1990. Each dot represents a specific month.

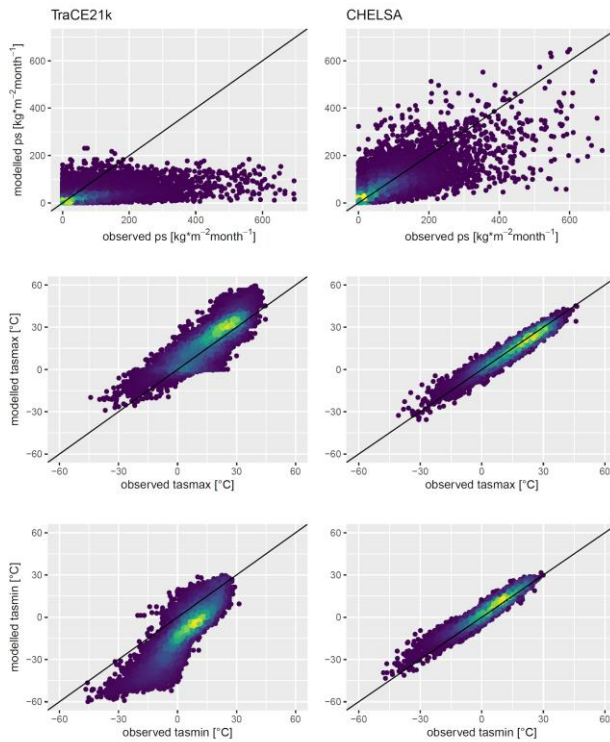


Figure 4: Scatter plots comparing precipitation, maximum, and minimum temperature. Data are aggregated from TraCE21k and CHELSA_TraCE21k for the 20th century time period with observational data from the Global Historical Climate Network (GHCN) for the time period 1900–1990.

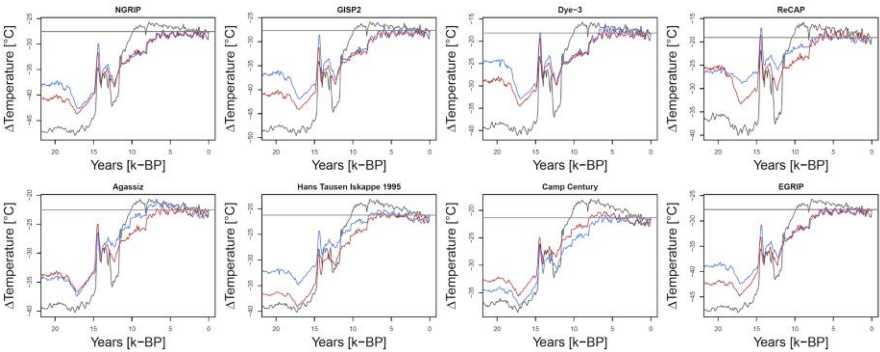
5.2 Performance of the downscaling algorithms for temperatures compared to ice cores

Compared to the temperature reconstructions, the downscaled CHELSA_TraCE21k model had reduced bias at four of the ice core sites located at the edges of the GIS (ReCAP, Agassiz, Hans Tausen Iskappe, Camp Century), but increased the bias; RMSE and MAE at the remaining four sites at the center of the GIS (NEEM, NGRIP, GISP2, Dye 3) (Fig. 5). Overall both CHELSA_TraCE as well as TraCE21k show a warm bias before the H1 event, and roughly after the 8.2k event at four of the sites (ReCAP, Agassiz, Hans Tausen Iskappe, Camp Century). At three sites (ReCAP, Agassiz, Hans Tausen Iskappe, Camp Century) a cold bias is present after the younger Dryas (Fig. 5). At the four other sites, the biases are idiosyncratic with

Formatted: Normal

660

CHELSA_TraCE usually showing a warm bias before the H1, and TraCE a cold bias before the H1 (Fig. 5). After the younger dryas, both models show a cold bias at these sites. At the Camp Century site, the Trace data are close to the $\delta^{15}\text{N}$ -based temperature reconstructions before the H1 event, and CHELSA_TraCE shows a warm bias, while after the younger dryas the situation is reversed (Fig. 5).



665

Figure 5: Comparison of temperature anomalies from current for the CHELSA-TraCE21k time series data (blue), the TraCE21k data (red), with the temperature reconstructions from ice cores (black) across Greenland. The grey line indicates the current observed temperature during the period 1981-2010 from CHELSA V2.1. Temperatures are plotted as anomalies from the current temperature recorded at the respective location of the ice cores.

670

5.3 Accuracy of the glacier extent between 18kBP and 1kBP

675

The test validations of the glacial extent show a good performance over most time steps (Fig. 6), but with a notable drop in accuracy at 8 kBP8k BP where all three-validation metrics drop significantly. Aside from the drop at 8 kBP8k BP, the performance of the glacial extent simulations performed well. The marked drop in performance around 8 kBP8k BP might be due to the 8.2 kiloyear2k event, which marked a strong decrease in global temperatures, most likely due to meltwater fluxes from the collapsing Laurentide ice sheet. The strong coupling between temperature and glacial extent in CHELSA-TraCE21k generates an increase in glacial extent more than a sudden collapse during this time period, which seems to override the signal from the ICE6G forcing data in CHELSA-TraCE21k.

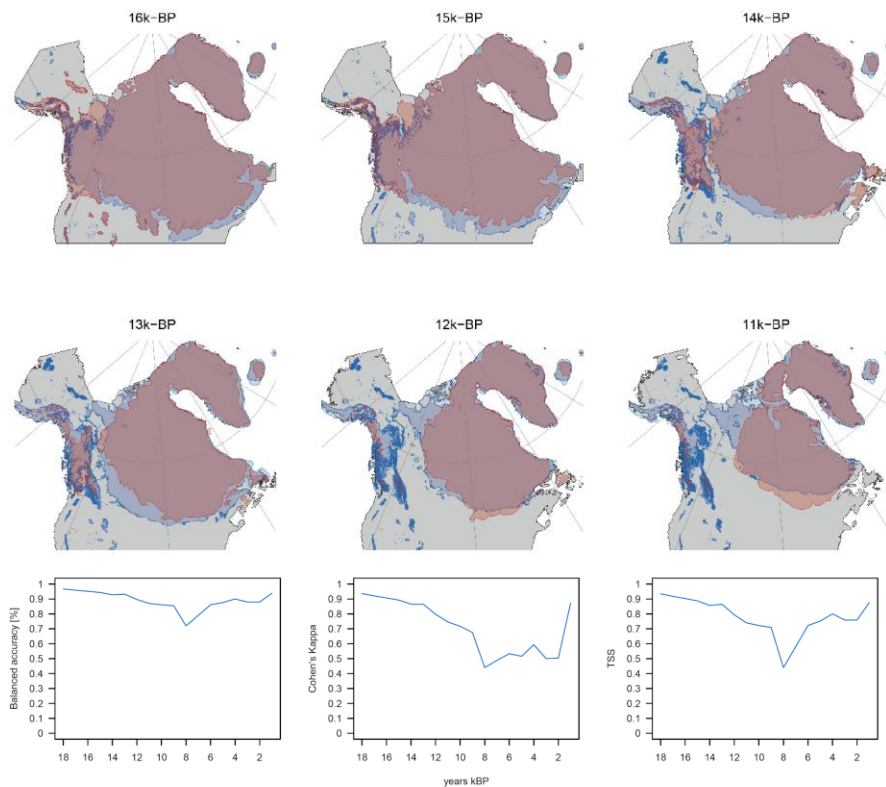


Figure 6: Comparisons of estimated glacial extents of the Laurentide ice shield from 16k-BP to 11k-BP. Blue delineates the interpolated ice shield extent from CHELSA-TraCE21k, and red shows the estimated extent from (Dyke et al., 2003). While the retreat of the main Laurentide ice shield is similar in both estimations, the Cordilleran Ice shield covering the Rocky Mountains, retreats faster in the estimations by (Dyke et al., 2003), compared to CHELSA-TraCE21. b.) Performance comparison using three different metrics (Balanced accuracy, Cohen's Kappa, and True Skill Statistic) from a comparison of CHELSA-TraCE21k and Dyke et al. 2003.

Formatted: Font: Bold

685 **6 Potential applications: Dynamic**Plausibility test using dynamic simulation of effective plant refugia

Transient long-term climatic data have a wide range of possible applications. Here we ~~want to highlight a possible~~use one application in paleo-ecology ~~by using a plausibility test to additionally check it~~ the ~~climate~~transient CHELSA-TraCE21k data is able to reliably detect known LGM refugia of plant species. Climatic changes during the last glacial cycle since the LGM, 690 have had a significant influence on the distribution of ecosystems (Williams and Jackson, 2007), ~~species (Hampe and Jump, 2011; Hewitt, 1999); and as a result on intraspecific genetic structures and speciation (Alsos et al., 2012; Pellissier et al., 2015; Yannie et al., 2014, 2020).~~ , species (Hewitt, 1999; Hampe and Jump, 2011), and as a result on intraspecific genetic structures and speciation (Alsos et al., 2012; Yannie et al., 2014, 2020; Pellissier et al., 2015).

695 Tracing the distribution of species through time is, however, challenging ~~as the~~ the spatio-temporal distributions of species strongly depend on environmental suitability (Guisan and Zimmermann, 2000), spatial accessibility of a given location ~~(Normand et al., 2011; Svenning and Skov, 2004)~~(Svenning and Skov, 2004; Normand et al., 2011), and species dispersal abilities (Engler and Guisan, 2009). A dynamic simulation of species distributions can integrate all these aspects and therefore provides a valuable testbed for ~~paleo~~climatic data (Nobis and Normand, 2014). However, the spatio-temporal 700 resolution of climate data needed for such simulations have been limited to comparable coarse grain climatic data (Gherghel and Martin, 2020), which usually creates a mismatch between the climate derived from the model and the climate actually experienced by an organism (Seo et al., 2009).

Here, we use the downscaled transient temperature and precipitation ~~data from~~ CHELSA-TraCE21 since ~~17kyBP~~17k BP (the 705 coldest recorded temperatures in the ~~TraCE21k~~CHELSA-TraCE21k model for Europe) to reconstruct refugia of the deciduous tree Grey Alder (*Alnus incana*) in Europe before post glacial climate warming. Similar to Nobis & Normand (2014), we first calibrated a generalized linear model (GLM) (Nelder and Wedderburn, 1972) using current presences and absences of Grey Alder within polygons of the Atlas Florae Europaeae (AFE) (Kurtto et al., 2018) as the response variable and current annual mean temperature and precipitation from CHELSA-TraCE21k as predictors calculated as zonal mean values of 5 x 5 km rasterized AFE polygons. Despite the simplicity of the model it showed a fair to good model fit with a 10-fold cross-validated 710 AUC value of 0.89.

Then, the GLM model was used to predict the suitability of Grey Alder from ~~17kyBP~~17k BP till today in 500-year steps with 5 km resolution and Lambert azimuthal equal-area projection. Glaciated areas were defined as unsuitable and were taken from the CHELSA-TraCE21k glacial reconstructions. We used the resulting time series of climatic suitability as input to the KISSMig (Keep it simple stupid migration) model (Nobis & Normand 2014), which iteratively uses a simple 3 x 3 cell 715 algorithm to calculate the spatial spread from a given origin ~~from 17kyBP~~from 17k BP to present. Presences and absences were weighted equally for the initial GLM calibration -and KISSMig used squared suitability values to ~~fulfill~~fulfil basic empirical expectations (see <http://purl.oclc.org/wsl/kissmig>).

Formatted: Font: Italic

Formatted: Font: Italic

We tested for each AFE polygon of the current Grey Alder distribution all 25 x 25 km areas across Europe as potential refugia. All 5 ~~5x5~~ km grid cells of those areas suitable at ~~17kyBP~~17k BP were kept as refugia, if the respective AFE polygon was accessible and the spread pattern generated the lowest number of false positives when compared to the current AFE distribution. Because the migration ability of Grey Alder was unknown a priori, KISSMig simulations used one to 10 iterations for each 500-year step, corresponding to a maximum migration rate of 10 to 100 m/~~yr~~a. For each iteration number, the combined spread pattern from all detected effective refugia was compared with the current distribution based on F1-scores. The optimized iteration number was identified by optimizing F1, which showed for Grey Alder a maximum migration rate of 50 m/~~yr~~a. For a comparison with genetic clusters (Dering et al., 2016), the locations of that study were linked to the detected effective refugia with the shortest euclidean distance for simplicity.

Current genetic clustering of populations indicates that the modelling of *A. incana* distributions at ~~17kyBP~~17k BP shows that simulations based on CHELSA-TraCE21k successfully detected glacial refugia in the Southern Alps, southern Norway, northern Norway, the Balkans, and eastern Romania (Fig. 7). The situation in eastern Europe is more complex, with most refugia located in Russia. However, since we only used the current distribution of *A. incana* in western Europe the results might be biased towards the east.

Formatted: Font: Italic

Formatted: Font: Italic

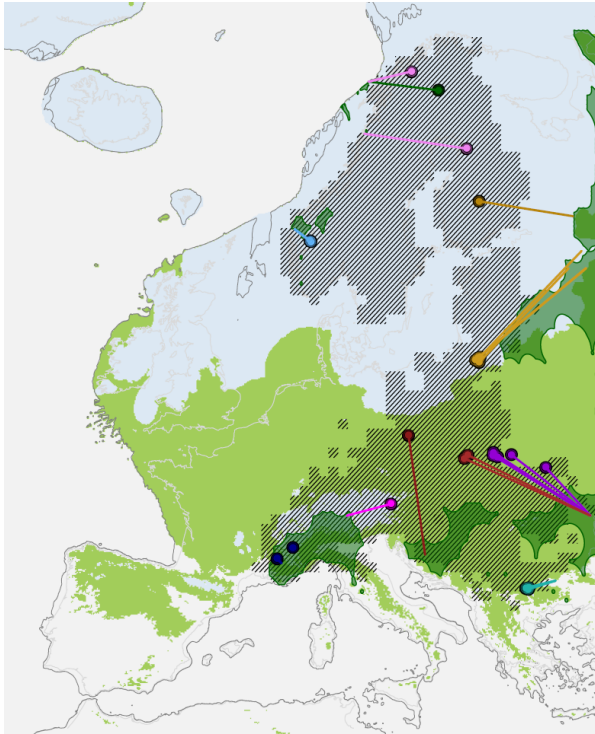


Figure 7: Distribution of *Alnus incana* in Europe (based on the Atlas Flora Europaea (Kurtto et al., 2018)) at current time (line shaded/hatched), and reconstructed effective refugia at 17k BP (dark green alpha hull polygons) using dynamic species distribution modelling based on KISSMig and CHELSA—TraCE21k. The entire suitable habitat for *A. incana* at 17k BP is indicated as light green. Although almost the entire southern-central Europe was suitable for *A. incana* at 17k BP, it might not have not been occurred at all locations due to dispersal constraints, which are considered in the dark green KissMig reconstructed distribution. Colored circles indicate the population genetic structure of *A. incana*, taken from Dering et al. 2016, where each color represents a genetic cluster. Lines indicate the most likely effective refugia a genetic cluster can be associated to, given dispersal and climatic constraints. Current genetic clustering of populations indicates that the modelling of *A. incana* distributions at 17k BP successfully detected glacial effective refugia in the Southern Alps (dark blue), southern Norway (light blue), northern Norway (pink), the Balkans (dark red), and eastern Romania (turquoise), and the black sea (dark red and violet). As we only use the current distribution of *A. incana* within the AFE extent the results might be biased outside of it.

Formatted: Font: Italic

7 Conclusions

Although both, the original [TraCE24k](#)[TraCE-21k](#), as well as the downscaled CHELSA-Trace21k data track the relative temperature change well compared to ice cores, both models have relatively high temperature biases in absolute temperatures. Both the original data and the downscaled data have a warm bias before the younger Dryas, and a cold bias after it relative to the ice core proxy data. There are several reasons for this: coupled atmosphere ocean general circulation models (GCMs) such as CCSM3 cannot provide regional-scale or unbiased information on a variety of climatic processes (Meehl et al., 2007).

Temperatures from ice cores themselves are only based on proxy data, and the overall performance of such proxy data in estimating absolute temperatures is connected to biases in itself (Erb et al., 2018). The downscaling of the CHELSA-Trace21k data involves a trend-preserving (Hempel et al., 2013) change factor step to explicitly preserve the trends in [TraCE24k](#)[TraCE-21k](#). If, however, these trends are already underestimated by the [TraCE24k](#)[TraCE-21k](#) data, they will also be present in the downscaled data.

The estimation of glacial extents ~~works comparably well when~~[shows an accuracy of >80%](#) compared to expert delineations of the glacial extent of the Laurentide ice ~~shield~~[sheet](#). There is, however, a clear drop in ~~performance~~[accuracy](#) at the ~~8.4kY~~[8k BP](#) event when atmospheric methane concentration decreased leading to a cooling and drying of the northern hemisphere (Kobashi et al., 2007). The strong coupling of the ice interpolations with only temperature might cause the decrease in performance as the downscaling algorithm ignores changes in precipitation ~~which is that are~~ only present in the driving ICE6G data. As the downscaling assumes an increase in glacial boundaries with cooling, this effect might not be realistic under an overall drying climate, and the fast shifts in temperatures over only 150 years (Kobashi et al., 2007) might also not be well represented in a model with 100 year resolution. Another problem in the estimation of the glacial extent might ~~be the result of~~[contain errors from](#) the applied B-spline interpolation. The resulting ice cover from this interpolation can, in some areas, only be a few meters thick, not representing real glaciers, but rather spatial autocorrelation artefact of the interpolation approach used.

The CHELSA-Trace21k data seems to be able to recreate the distribution of temperature and precipitation in a meaningful manner, so that the use of the data in subsequent analysis produces meaningful results. The reconstruction of the refugia for *Alnus incana* shows that the combination of high-resolution climate data, together with a dynamic distribution model was able to accurately detect refugia, even those of a few ~~kilometers~~[kilometer](#) in extent (Parducci et al., 2012) that cannot be detected using coarse climate data.

Code availability

Downscaling codes are based on (Karger et al., 2017a), and all modules used are open source and integrated into SAGA-GIS, available here: <https://sourceforge.net/projects/saga-gis/>. The code unique to this study is written in R and creates the paleo-orography and glacier interpolations, and is also available on zenodo (DOI:10.5281/zenodo.4545753).

Data availability

775 All post-processed data ([Karger et al., 2021](#))([Karger et al., 2021a](#)) and additional input files other than those provided by
TraCE21k can be accessed at the envidat.ch (DOI:10.16904/envidat.211.). The data is published under a Creative Commons
Attribution 2.0 Generic (CC BY 2.0) license.

Author contribution

D.N.K., M.N., and N.Z. developed the idea. D.N.K. developed the model and implemented the code. D.N.K. M.N. and S.N.
780 validated the data. N.Z., S.N., and C.H.G. funded the project. D.N.K. wrote the first version of the manuscript and all authors
contributed to subsequent revisions.

Competing interest

The authors declare that they have no conflict of interest.

Acknowledgements

785 D.N.K. & N.E.Z. acknowledge funding from: The WSL internal grants exCHELSA and ClimEx, the Joint Biodiversa
COFUND Call on “Biodiversity and Climate Change” (project ‘FeedBaCks’) with the national funder Swiss National
Foundation (20BD21_193907), as well as the Swiss Data Science Projects: SPEEDMIND, and COMECO. D.N.K. & C.H.G.
acknowledges funding to the ERA-Net BiodivERsA - Belmont Forum, with the national funder Swiss National Foundation
(20BD21_184131), part of the 2018 Joint call BiodivERsA-Belmont Forum call (project ‘FutureWeb’), the WSL internal grant
790 ClimEx. S.N. acknowledge funding from Aarhus University Research Foundation.

References

Adams, J. M. and Faure, H.: Preliminary Vegetation Maps of the World since the Last Glacial Maximum: An Aid to
Archaeological Understanding, *J. Archaeol. Sci.*, 24(7), 623–647, <https://doi.org/10.1006/jasc.1996.0146>, 1997.

Allouche, O., Tsoar, A., and Kadmon, R.: Assessing the accuracy of species distribution models: prevalence, kappa and the
795 true skill statistic (TSS), *J. Appl. Ecol.*, 43(6), 1223–1232, <https://doi.org/10.1111/j.1365-2664.2006.01214.x>, 2006.

Alsos, I. G., Ehrich, D., Thuiller, W., Eidesen, P. B., Tribsch, A., Schönswetter, P., Lagaye, C., Taberlet, P., and
Brochmann, C.: Genetic consequences of climate change for northern plants, *Proc. R. Soc. B Biol. Sci.*, 279(1735), 2042–
2051, <https://doi.org/10.1098/rspb.2011.2363>, 2012.

Argus, D. F., Peltier, W. R., Drummond, R., and Moore, A. W.: The Antarctica component of postglacial rebound model
800 ICE-6G_C (VM5a) based on GPS positioning, exposure age dating of ice thicknesses, and relative sea level histories,
Geophys. J. Int., 198, 537–563, <https://doi.org/10.1093/gji/ggu140>, 2014.

Formatted: Font: Times New Roman, 10 pt

- Basist, A., Bell, G. D., and Meentemeyer, V.: Statistical Relationships between Topography and Precipitation Patterns, *J. Clim.*, 7(9), 1305–1315, [https://doi.org/10.1175/1520-0442\(1994\)007<1305:SRBTAP>2.0.CO;2](https://doi.org/10.1175/1520-0442(1994)007<1305:SRBTAP>2.0.CO;2), 1994.
- 805 Berrisford, P., Dee, D., Fielding, K., Fuentes, M., Kallberg, P., Kobayashi, S., and Uppala, S.: The ERA-interim archive, *ERA Rep. Ser.*, (4), 1–16, 2009.
- [Biasutti, M., Yuter, S. E., Burleyson, C. D. and Sobel, A. H.: Very high resolution rainfall patterns measured by TRMM precipitation radar: seasonal and diurnal cycles, *Clim. Dyn.*, 39\(1–2\), 239–258, <https://doi.org/10.1007/s00382-011-1146-6>, 2011.](#)
- 810 Binney, H., Edwards, M., Macias-Fauria, M., Lozhkin, A., Anderson, P., Kaplan, J. O., Andreev, A., Bezrukova, E., Blyakharchuk, T., Jankovska, V., Khazina, I., Krivonogov, S., Kremenetski, K., Nield, J., Novenko, E., Ryabogina, N., Solovieva, N., Willis, K., and Zernitskaya, V.: Vegetation of Eurasia from the last glacial maximum to present: Key biogeographic patterns, *Quat. Sci. Rev.*, 157, 80–97, <https://doi.org/10.1016/j.quascirev.2016.11.022>, 2017.
- Böhner, J.: General climatic controls and topoclimatic variations in Central and High Asia, *Boreas*, 35(2), 279–295, <https://doi.org/10.1111/j.1502-3885.2006.tb01158.x>, 2006.
- 815 Böhner, J. and Antonic, O.: Böhner, J., & Antonic, O. (2009). Land-Surface Parameters Specific to Topo-Climatology. In T. Hengl, & H. I. Reuter (Eds.), *GEOMORPHOMETRY: CONCEPTS, SOFTWARE, APPLICATIONS* (pp. 195–226). Elsevier Science., in: in T. Hengl, & H. I. Reuter (eds.) *Geomorphometry: Concepts, Software, Applications*, pp. 195–226, Elsevier Science., 195–226, 2009.
- 820 Brown, J. L., Hill, D. J., Dolan, A. M., Carnaval, A. C., and Haywood, A. M.: PaleoClim, high spatial resolution paleoclimate surfaces for global land areas, *Sci. Data*, 5(4), 1–9, <https://doi.org/10.1038/sdata.2018.254>, 2018.
- Buizert, C., Gkinis, V., Severinghaus, J. P., He, F., Lecavalier, B. S., Kindler, P., Leuenberger, M., Carlson, A. E., Vinther, B., Masson-Delmotte, V., White, J. W. C., Liu, Z., Otto-Bliesner, B., and Brook, E. J.: Greenland temperature response to climate forcing during the last deglaciation, *Science*, 345(6204), 1177–1180, <https://doi.org/10.1126/science.1254961>, 2014.
- 825 Buizert, C., Keisling, B. A., Box, J. E., He, F., Carlson, A. E., Sinclair, G., and DeConto, R. M.: Greenland-Wide Seasonal Temperatures During the Last Deglaciation, *Geophys. Res. Lett.*, 45(4), 1905–1914, <https://doi.org/10.1002/2017GL075601>, 2018.
- Carlson, A. E., Ullman, D. J., Anslow, F. S., He, F., Clark, P. U., Liu, Z., and Otto-Bliesner, B. L.: Modeling the surface mass-balance response of the Laurentide Ice Sheet to Bølling warming and its contribution to Meltwater Pulse 1A, *Earth Planet. Sci. Lett.*, 315–316, 24–29, <https://doi.org/10.1016/j.epsl.2011.07.008>, 2012.
- 830 [Collins, W. D., Bitz, C. M., Blackmon, M. L., Bonan, G. B., Bretherton, C. S., Carton, J. A., Chang, P., Doney, S. C., Hack, J. J., Henderson, T. B., Kiehl, J. T., Large, W. G., McKenna, D. S., Santer, B. D. and Smith, R. D.: The Community Climate System Model Version 3 \(CCSM3\), *J. Clim.*, 19\(11\), 2122–2143, <https://doi.org/10.1175/JCLI3761.1>, 2006.](#)
- Daly, C., Taylor, G. H., and Gibson, W. P.: The PRISM approach to mapping precipitation and temperature, *Proc 10th AMS Conf Appl. Climatol.*, 20–23, 1997.
- 835 Danielson, J. J. and Gesch, D. B.: Global multi-resolution terrain elevation data 2010 (GMTED2010), US Geological Survey, 2011.
- Dyke, A. S., Moore, A., and Robertson, L.: Deglaciation of North America, 2003.

Ehlers, J., Gibbard, P. L. and Hughes, P. D.: Quaternary Glaciations - Extent and Chronology, Volume 15 - 1st Edition, 2011.

840 Engler, R. and Guisan, A.: MigClim: Predicting plant distribution and dispersal in a changing climate, Divers. Distrib., 15(4), 590–601, <https://doi.org/10.1111/j.1472-4642.2009.00566.x>, 2009.

Erb, M. P., Jackson, C. S., Broccoli, A. J., Lea, D. W., Valdes, P. J., Crucifix, M. and DiNezio, P. N.: Model evidence for a seasonal bias in Antarctic ice cores, Nat. Commun., 9(1), 1361, <https://doi.org/10.1038/s41467-018-03800-0>, 2018.

845 Frei, C. and Schär, C.: A precipitation climatology of the Alps from high-resolution rain-gauge observations, Int. J. Climatol., 18(8), 873–900, [https://doi.org/10.1002/\(SICI\)1097-0088\(19980630\)18:8<873::AID-JOC255>3.0.CO;2-9](https://doi.org/10.1002/(SICI)1097-0088(19980630)18:8<873::AID-JOC255>3.0.CO;2-9), 1998.

850 Frieler, K., Lange, S., Piontek, F., Reyer, C. P. O., Schewe, J., Warszawski, L., Zhao, F., Chini, L., Denvil, S., Emanuel, K., Geiger, T., Halladay, K., Hurtt, G., Mengel, M., Murakami, D., Ostberg, S., Popp, A., Riva, R., Stevanovic, M., Suzuki, T., Volkholz, J., Burke, E., Ciais, P., Ebi, K., Eddy, T. D., Elliott, J., Galbraith, E., Gosling, S. N., Hattermann, F., Hickler, T., Hinkel, J., Hof, C., Huber, V., Jägermeyr, J., Krysanova, V., Marcé, R., Müller Schmied, H., Mouratiadou, I., Pierson, D., Tittensor, D. P., Vautard, R., Vliet, M. van, Biber, M. F., Betts, R. A., Bodirsky, B. L., Deryng, D., Frolking, S., Jones, C. D., Lotze, H. K., Lotze-Campen, H., Sahajpal, R., Thonicke, K., Tian, H. and Yamagata, Y.: Assessing the impacts of 1.5 °C global warming – simulation protocol of the Inter-Sectoral Impact Model Intercomparison Project (ISIMIP2b), Geosci. Model Dev., 10(12), 4321–4345, <https://doi.org/10.5194/gmd-10-4321-2017>, 2017.

855 Fuhrer, O., Chadha, T., Hoefler, T., Kwasniewski, G., Lapillonne, X., Leutwyler, D., Lüthi, D., Osuna, C., Schär, C., Schulthess, T. C. and Vogt, H.: Near-global climate simulation at 1km resolution: establishing a performance baseline on 4888 GPUs with COSMO 5.0, Geosci. Model Dev., 11(4), 1665–1681, <https://doi.org/10.5194/gmd-11-1665-2018>, 2018.

[Funk, C., Verdin, A., Michaelsen, J., Peterson, P., Pedreros, D. and Husak, G.: A global satellite-assisted precipitation climatology, Earth Syst Sci Data, 7\(2\), 275–287, https://doi.org/10.5194/essd-7-275-2015, 2015.](https://doi.org/10.5194/essd-7-275-2015)

860 Gao, X., Xu, Y., Zhao, Z., Pal, J. S. and Giorgi, F.: On the role of resolution and topography in the simulation of East Asia precipitation, Theor. Appl. Climatol., 86(1–4), 173–185, <https://doi.org/10.1007/s00704-005-0214-4>, 2006.

Gherghel, I. and Martin, R. A.: Postglacial recolonization of North America by spadefoot toads: integrating niche and corridor modeling to study species' range dynamics over geologic time, Ecography, 43(10), 1499–1509, <https://doi.org/10.1111/ecog.04942>, 2020.

865 Guisan, A. and Thuiller, W.: Predicting species distribution: offering more than simple habitat models, Ecol. Lett., 8(9), 993–1009, 2005.

Guisan, A. and Zimmermann, N. E.: Predictive habitat distribution models in ecology, Ecol. Model., 135, 147–186, 2000.

Hampe, A. and Jump, A. S.: Climate Relicts: Past, Present, Future, Annu. Rev. Ecol. Evol. Syst., 42(1), 313–333, <https://doi.org/10.1146/annurev-ecolsys-102710-145015>, 2011.

870 Harris, I., Osborn, T. J., Jones, P. and Lister, D.: Version 4 of the CRU TS monthly high-resolution gridded multivariate climate dataset, Sci. Data, 7(1), 1–18, <https://doi.org/10.1038/s41597-020-0453-3>, 2020.

He, F.: Simulating Transient Climate Evolution of the Last Deglaciation with CCSM3, PhD - Thesis, University of Wisconsin Madison, Madison, WC, USA, 171 pp., 2011.

- Hempel, S., Frieler, K., Warszawski, L., Schewe, J., and Piontek, F.: A trend-preserving bias correction–the ISI-MIP approach, *Earth Syst. Dyn.*, 4(2), 219–236, 2013.
- 875 Hewitt, G. M.: Post-glacial re-colonization of European biota, *Biol. J. Linn. Soc.*, 68(1–2), 87–112, <https://doi.org/10.1111/j.1095-8312.1999.tb01160.x>, 1999.
- Hijmans, R. J., Cameron, S. E., Parra, J. L., Jones, P. G., and Jarvis, A.: Very high resolution interpolated climate surfaces for global land areas, *Int. J. Climatol.*, 25(15), 1965–1978, <https://doi.org/10.1002/joc.1276>, 2005.
- 880 Huffman, G. J., Bolvin, D. T., Nelkin, E. J., Wolff, D. B., Adler, R. F., Gu, G., Hong, Y., Bowman, K. P. and Stecker, E. F.: The TRMM Multisatellite Precipitation Analysis (TMPA): Quasi-Global, Multiyear, Combined Sensor Precipitation Estimates at Fine Scales, *J. Hydrometeorol.*, 8(1), 38–55, <https://doi.org/10.1175/JHM560.1>, 2007.
- Hunter, R. D. and Meentemeyer, R. K.: Climatologically Aided Mapping of Daily Precipitation and Temperature, *J. Appl. Meteorol.*, 44(10), 1501–1510, <https://doi.org/10.1175/JAM2295.1>, 2005.
- 885 Hutchinson, G. E.: POPULATION STUDIES - ANIMAL ECOLOGY AND DEMOGRAPHY - CONCLUDING REMARKS, *Cold Spring Harb. Symp. Quant. Biol.*, 22, 415–427, 1957.
- Karger, D. N., Conrad, O., Böhner, J., Kawohl, T., Kreft, H., Soria-Auza, R. W., Zimmermann, N. E., Linder, H. P., and Kessler, M.: Climatologies at high resolution for the earth’s land surface areas, *Sci. Data*, 4, 170122, 2017a.
- Karger, D. N., Conrad, O., Böhner, J., Kawohl, T., Kreft, H., Soria-Auza, R. W., Zimmermann, N. E., Linder, H. P., and Kessler, M.: Climatologies at high resolution for the earth’s land surface areas, *Dryad Digital Repository*, <https://doi.org/10.5061/dryad.kd1d4>, 2017b.
- 890 Karger, D. N., Schmatz, D. R., Dettling, G., and Zimmermann, N. E.: High resolution monthly precipitation and temperature timeseries for the period 2006-2100, *Sci. Data*, 2020.
- Karger, D. N., Nobis, M., Normand, S., Graham, C. H., and Zimmermann, N. E.: CHELSA-TraCE21k: Downscaled transient temperature and precipitation data since the last glacial maximum - EnviDat, *envidat*, <https://doi.org/10.16904/envidat.211>, 2021a.
- Karger, D. N., Wilson, A. M., Mahony, C., Zimmermann, N. E., and Jetz, W.: Global daily 1 km land surface precipitation based on cloud cover-informed downscaling, *Sci. Data*, 8, 307, <https://doi.org/10.1038/s41597-021-01084-6>, 2021b.
- Kobashi, T., Severinghaus, J. P., Brook, E. J., Barnola, J.-M., and Grachev, A. M.: Precise timing and characterization of abrupt climate change 8200 years ago from air trapped in polar ice, *Quat. Sci. Rev.*, 26(9), 1212–1222, <https://doi.org/10.1016/j.quascirev.2007.01.009>, 2007.
- 900 Körner, C.: The use of ‘altitude’ in ecological research, *Trends Ecol. Evol.*, 22(11), 569–574, <https://doi.org/10.1016/j.tree.2007.09.006>, 2007.
- Kurtto, A., Sennikov, A. B., and Lampinen, R.: Atlas Florae Europaeae - Distribution of vascular plants in Europe, *Comm. Mapp. Flora Eur. Soc. Biol. Fenn. Vanamo Hels.* 132 Pp, 23(1), 106–106, 2018.
- 905 Lawrence, M. G.: The Relationship between Relative Humidity and the Dewpoint Temperature in Moist Air: A Simple Conversion and Applications, *Bull. Am. Meteorol. Soc.*, 86(2), 225–234, <https://doi.org/10.1175/BAMS-86-2-225>, 2005.

- Lawrimore, J. H., Menne, M. J., Gleason, B. E., Williams, C. N., Wuertz, D. B., Vose, R. S. and Rennie, J.: An overview of the Global Historical Climatology Network monthly mean temperature data set, version 3, *J. Geophys. Res.-Atmospheres*, 116(~~D19121~~), D19121, <https://doi.org/10.1029/2011jd016187>, 2011.
- 910 Liu, M., Bárdossy, A. and Zehe, E.: Interaction of valleys and circulation patterns (CPs) on small-scale spatial precipitation distribution in the complex terrain of southern Germany., *Hydrol. Earth Syst. Sci. Discuss.*, 9(~~42~~), 2012.
- Liu, Z., Otto-Bliesner, B. L., He, F., Brady, E. C., Tomas, R., Clark, P. U., Carlson, A. E., Lynch-Stieglitz, J., Curry, W., Brook, E., Erickson, D., Jacob, R., Kutzbach, J. and Cheng, J.: Transient Simulation of Last Deglaciation with a New Mechanism for Bølling-Allerød Warming, *Science*, 325(~~5938~~), 310–314, <https://doi.org/10.1126/science.1171041>, 2009.
- 915 Maraun, D.: Bias correction, quantile mapping, and downscaling: Revisiting the inflation issue, *J. Clim.*, 26(~~6~~), 2137–2143, 2013.
- Maraun, D.: Bias Correcting Climate Change Simulations - a Critical Review, *Curr. Clim. Change Rep.*, 2(~~4~~), 211–220, <https://doi.org/10.1007/s40641-016-0050-x>, 2016.
- Maraun, D., Wetterhall, F., Ireson, A. M., Chandler, R. E., Kendon, E. J., Widmann, M., Brienens, S., Rust, H. W., Sauter, T., Themeßl, M., Venema, V. K. C., Chun, K. P., Goodess, C. M., Jones, R. G., Onof, C., Vrac, M. and Thiele-Eich, I.: Precipitation downscaling under climate change: Recent developments to bridge the gap between dynamical models and the end user, *Rev. Geophys.*, 48(~~3~~), RG3003, <https://doi.org/10.1029/2009RG000314>, 2010.
- Marcott, S. A., Clark, P. U., Padman, L., Klinkhammer, G. P., Springer, S. R., Liu, Z., Otto-Bliesner, B. L., Carlson, A. E., Ungerer, A., Padman, J., He, F., Cheng, J. and Schmittner, A.: Ice-shelf collapse from subsurface warming as a trigger for Heinrich events, *Proc. Natl. Acad. Sci.*, 108(~~33~~), 13415–13419, <https://doi.org/10.1073/pnas.1104772108>, 2011.
- 925 McMaster, G. S. and Wilhelm, W.: Growing degree-days: one equation, two interpretations, 1997.
- Meehl, G. A., Stocker, T. F., Collins, W. D., Friedlingstein, P., Gaye, A. T., Gregory, J. M., Kitoh, A., Knutti, R., Murphy, J. M., Noda, A., Raper, S. C. B., Watterson, I. G., Weaver, A. J. and Zhao, Z.-C.: Global climate projections, in: *Climate Change 2007: The Physical Science Basis. Contribution of Working Group I to the Fourth Assessment Report of the Intergovernmental Panel on Climate Change*, Cambridge University Press, Cambridge, UK, 2007.
- 930 Meyer-Christoffer, A., Becker, A., Finger, P., Rudolf, B., Schneider, U. and Ziese, M.: GPCC Climatology Version 2015 at 0.25°: Monthly Land-Surface Precipitation Climatology for Every Month and the Total Year from Rain-Gauges built on GTS-based and Historic Data., *Glob. Precip. Climatol. Cent. GPCC*, https://doi.org/10.5676/DWD_GPCC/CLIM_M_V2015_025, 2015.
- 935 Miller, K. G., Kominz, M. A., Browning, J. V., Wright, J. D., Mountain, G. S., Katz, M. E., Sugarman, P. J., Cramer, B. S., Christie-Blick, N. and Pekar, S. F.: The Phanerozoic Record of Global Sea-Level Change, *Science*, 310(~~5752~~), 1293–1298, <https://doi.org/10.1126/science.1116412>, 2005.
- Nelder, J. A. and Wedderburn, R. W. M.: Generalized Linear Models, *J. R. Stat. Soc. Ser. Gen.*, 135(~~3~~), 370–384, <https://doi.org/10.2307/2344614>, 1972.
- 940 Neumann, P., Düben, P., Adamidis, P., Bauer, P., Brück, M., Kornblueh, L., Klocke, D., Stevens, B., Wedi, N. and Biercamp, J.: Assessing the scales in numerical weather and climate predictions: will exascale be the rescue?, *Philos. Trans. R. Soc. Math. Phys. Eng. Sci.*, 377(~~2142~~), 20180148, <https://doi.org/10.1098/rsta.2018.0148>, 2019.

- Nobis, M. P. and Normand, S.: KISSMig – a simple model for R to account for limited migration in analyses of species distributions, *Ecography*, 37(42), 1282–1287, <https://doi.org/10.1111/ecog.00930>, 2014.
- 945 Normand, S., Ricklefs, R. E., Skov, F., Bladt, J., Tackenberg, O., and Svenning, J.-C.: Postglacial migration supplements climate in determining plant species ranges in Europe, *Proc. R. Soc. Lond. B Biol. Sci.*, rspb20102769, <https://doi.org/10.1098/rspb.2010.2769>, 2011.
- Oke, T. R.: *Boundary layer climates*, Routledge, 464 pp., 2002.
- 950 Otto-Bliesner, B. L., Brady, E. C., Clauzet, G., Tomas, R., Levis, S., and Kothavala, Z.: Last Glacial Maximum and Holocene Climate in CCSM3, *J. Clim.*, 19(44), 2526–2544, <https://doi.org/10.1175/JCLI3748.1>, 2006.
- Pellissier, L., Eidesen, P. B., Ehrich, D., Descombes, P., Schönschwetter, P., Tribsch, A., Westergaard, K. B., Alvarez, N., Guisan, A., Zimmermann, N. E., Normand, S., Vittoz, P., Luoto, M., Damgaard, C., Brochmann, C., Wisz, M. S., and Alsos, I. G.: Past climate-driven range shifts and population genetic diversity in arctic plants, *J. Biogeogr.*, n/a-n/a, <https://doi.org/10.1111/jbi.12657>, 2015.
- 955 Peltier, W. R.: Global glacial isostasy and the surface of the ice-age earth: The ICE-5G (CM2) Model and GRACE, *Annu. Rev. Earth Planet. Sci.*, 32(4), 111–149, <https://doi.org/10.1146/annurev.earth.32.082503.144359>, 2004.
- Peltier, W. R., Argus, D. F., and Drummond, R.: Space geodesy constrains ice age terminal deglaciation: The global ICE-6G_C (VM5a) model, *J. Geophys. Res. Solid Earth*, 120(4), 450–487, <https://doi.org/10.1002/2014JB011176>, 2015.
- 960 Prentice, I. C., Bartlein, P. J., and Webb, T.: Vegetation and Climate Change in Eastern North America Since the Last Glacial Maximum, *Ecology*, 72(6), 2038–2056, <https://doi.org/10.2307/1941558>, 1991.
- Raup, B., Racoviteanu, A., Khalsa, S. J. S., Helm, C., Armstrong, R., and Arnaud, Y.: The GLIMS geospatial glacier database: A new tool for studying glacier change, *Glob. Planet. Change*, 56(4), 101–110, <https://doi.org/10.1016/j.gloplacha.2006.07.018>, 2007.
- 965 Rotunno, R. and Houze, R. A.: Lessons on orographic precipitation from the Mesoscale Alpine Programme, *Q. J. R. Meteorol. Soc.*, 133(625), 811–830, <https://doi.org/10.1002/qj.67>, 2007.
- Schär, C., Fuhrer, O., Arteaga, A., Ban, N., Charpiloz, C., Di Girolamo, S., Hentgen, L., Hoefler, T., Lapillonne, X., Leutwyler, D., Osterried, K., Panosetti, D., Rüdüsühli, S., Schlemmer, L., Schulthess, T., Sprenger, M., Ubbiali, S., and Wernli, H.: Kilometer-scale climate models: Prospects and challenges, *Bull. Am. Meteorol. Soc.*, 101(5), <https://doi.org/10.1175/BAMS-D-18-0167.1>, 2019.
- 970 Schmidli, J., Frei, C., and Vidale, P. L.: Downscaling from GCM precipitation: a benchmark for dynamical and statistical downscaling methods, *Int. J. Climatol.*, 26(5), 679–689, <https://doi.org/10.1002/joc.1287>, 2006.
- Schulthess, T. C., Bauer, P., Wedi, N., Fuhrer, O., Hoefler, T., and Schär, C.: Reflecting on the goal and baseline for exascale computing: a roadmap based on weather and climate simulations, *Comput. Sci. Eng.*, 21(4), 30–41, 2018.
- Scotese, C. R.: *Atlas of earth history, PALEOMAP project*, 2001.
- 975 Seo, C., Thorne, J. H., Hannah, L., and Thuiller, W.: Scale effects in species distribution models: implications for conservation planning under climate change, *Biol. Lett.*, 5(4), 39–43, <https://doi.org/10.1098/rsbl.2008.0476>, 2009.

- Sepulchre, P., Caubel, A., Ladant, J.-B., Bopp, L., Boucher, O., Braconnot, P., Brockmann, P., Cozic, A., Donnadieu, Y., Dufresne, J.-L., Estella-Perez, V., Ethé, C., Fluteau, F., Foujols, M.-A., Gastineau, G., Ghattas, J., Hauglustaine, D., Hourdin, F., Kageyama, M., Khodri, M., Marti, O., Meurdesoif, Y., Mignot, J., Sarr, A.-C., Servonnat, J., Swingedouw, D., Szopa, S., and Tardif, D.: IPSL-CM5A2 – an Earth system model designed for multi-millennial climate simulations, *Geosci. Model Dev.*, 13(7), 3011–3053, <https://doi.org/10.5194/gmd-13-3011-2020>, 2020.
- Sevruk, B.: Regional Dependency of Precipitation-Altitude Relationship in the Swiss Alps, in: *Climatic Change at High Elevation Sites*, edited by H. F. Diaz, M.-H. F. Beniston, M., and R. S. Bradley, pp. 123–137, R. S., Springer Netherlands, 123–137, https://doi.org/10.1007/978-94-015-8905-5_7, 1997.
- Skamarock, C., Klemp, B., Dudhia, J., Gill, O., Liu, Z., Berner, J., Wang, W., Powers, G., Duda, G., Barker, D., and Huang, X.: A Description of the Advanced Research WRF Model Version 4, OpenSky, <https://doi.org/10.5065/1dfh-6p97>, 2019.
- Soria-Auza, R. W., Kessler, M., Bach, K., Barajas-Barbosa, P. M., Lehnert, M., Herzog, S. K., and Bohner, J.: Impact of the quality of climate models for modelling species occurrences in countries with poor climatic documentation: a case study from Bolivia, *Ecol. Model.*, 221(8), 1221–1229, 2010.
- Spreen, W. C.: A determination of the effect of topography upon precipitation, *Eos Trans. Am. Geophys. Union*, 28(2), 285–290, <https://doi.org/10.1029/TR028i002p00285>, 1947.
- Stull, R. B.: An introduction to boundary layer meteorology, Springer Science & Business Media, 2012.
- Svenning, J.-C. and Skov, F.: Limited filling of the potential range in European tree species, *Ecol. Lett.*, 7(7), 565–573, <https://doi.org/10.1111/j.1461-0248.2004.00614.x>, 2004.
- Velichko, A. A., Andreev, A. A., and Klimanov, V. A.: Climate and vegetation dynamics in the tundra and forest zone during the late glacial and holocene, *Quat. Int.*, 41–42, 71–96, [https://doi.org/10.1016/S1040-6182\(96\)00039-0](https://doi.org/10.1016/S1040-6182(96)00039-0), 1997.
- [Weatherall, P., Marks, K. M., Jakobsson, M., Schmitt, T., Tani, S., Arndt, J. E., Rovere, M., Chayes, D., Ferrini, V., and Wigley, R.: A new digital bathymetric model of the world's oceans, *Earth Space Sci.*, 2, 331–345, <https://doi.org/10.1002/2015EA000107>, 2015.](https://doi.org/10.1002/2015EA000107)
- Weischet, W. and Endlicher, W.: Einführung in die Allgemeine Klimatologie, Schweizerbart Science Publishers, Stuttgart, Germany, <https://www.schweizerbart.de/publications/detail/isbn/9783443071424/Einführung-in-die-Allgemeine-Klimatologie>, last access: 20 June 2020, 342 pp., 2008.
- Wilby, R. L., Wigley, T. M. L., Conway, D., Jones, P. D., Hewitson, B. C., Main, J., and Wilks, D. S.: Statistical downscaling of general circulation model output: A comparison of methods, *Water Resour. Res.*, 34(11), 2995–3008, <https://doi.org/10.1029/98WR02577>, 1998.
- Williams, J. W. and Jackson, S. T.: Novel climates, no-analog communities, and ecological surprises, *Front. Ecol. Environ.*, 5(9), 475–482, 2007.
- Williams, J. W., Shuman, B. N., III, T. W., Bartlein, P. J., and Leduc, P. L.: Late-Quaternary Vegetation Dynamics in North America: Scaling from Taxa to Biomes, *Ecol. Monogr.*, 74(2), 309–334, 2004.
- Willmott, C. J. and Robeson, S. M.: Climatologically aided interpolation (CAI) of terrestrial air temperature, *Int. J. Climatol.*, 15(2), 221–229, <https://doi.org/10.1002/joc.3370150207>, 1995.

Wood, A. W., Leung, L. R., Sridhar, V. and Lettenmaier, D. P.: Hydrologic Implications of Dynamical and Statistical Approaches to Downscaling Climate Model Outputs, *Clim. Change*, 62(1–3), 189–216, <https://doi.org/10.1023/B:CLIM.0000013685.99609.9e>, 2004.

015 Woodward, F. I., Fogg, G. E., Heber, U., Laws, R. M. and Franks, F.: The impact of low temperatures in controlling the geographical distribution of plants, *Philos. Trans. R. Soc. Lond. B Biol. Sci.*, 326(1237), 585–593, <https://doi.org/10.1098/rstb.1990.0033>, 1990.

Yannic, G., Pellissier, L., Ortego, J., Lecomte, N., Couturier, S., Cuyler, C., Dussault, C., Hundertmark, K. J., Irvine, R. J., Jenkins, D. A., Kolpashikov, L., Mager, K., Musiani, M., Parker, K. L., Røed, K. H., Sipko, T., Pórisson, S. G., Weckworth, B. V., Guisan, A., Bernatchez, L. and Côté, S. D.: Genetic diversity in caribou linked to past and future climate change, *Nat. Clim. Change*, 4(2), 132–137, <https://doi.org/10.1038/nclimate2074>, 2014.

020 Yannic, G., Hagen, O., Leugger, F., Karger, D. N. and Pellissier, L.: Harnessing paleo-environmental modeling and genetic data to predict intraspecific genetic structure, *Evol. Appl.*, 13(6), 1526–1542, <https://doi.org/10.1111/eva.12986>, 2020.

Yu, Z., Loisel, J., Brosseau, D. P., Beilman, D. W. and Hunt, S. J.: Global peatland dynamics since the Last Glacial Maximum, *Geophys. Res. Lett.*, 37(13), <https://doi.org/10.1029/2010GL043584>, 2010.

025